https://doi.org/10.5194/egusphere-2026-2470
Preprint. Discussion started: 25 August 2026

Instantaneous Response of a Tectonic–Fluvial–Lithologic Coupled System to Extreme Rainfall: Evidence From the 2023 Jinyang Torrent Event, China

Zhenkui Gu[1, 2, *], Xin Yao[1, 2], Xuchao Zhu[3], Junpeng Lou[4, *]

[1]Institute of Geomechanics, Chinese Academy of Geological Sciences, Beijing 100081, China
[2]Key Laboratory of Active Tectonics and Geological Safety, Ministry of Natural Resources, Beijing 100081, China
[3]State Key Laboratory of Soil and Sustainable Agriculture, Institute of Soil Science, Chinese Academy of Sciences, Nanjing 210008, China
[4]Chinalco Environmental Protection and Energy Conservation Group Corporation Limited, Beijing 102209, China

Correspondence to: Zhenkui Gu (guzhenkui15@mails.ucas.ac.cn) and Junpeng Lou (loujp.2019@tsinghua.org.cn)

Abstract. Under ongoing climate warming, extreme rainfall is becoming increasingly frequent, intensifying hazard pressure in mountainous regions where short-lived torrent events interact with long-term geomorphic evolution. Yet it remains unclear how external climatic forcing couples with the long-term antagonism between tectonic uplift and fluvial incision, and whether this coupled relationship can help identify hazard-prone geomorphic settings at the catchment scale. Here we investigate the 21 August 2023 torrent disaster in Jinyang County, Sichuan Province, China, as a representative case. Using multi-source data and quantitative analysis, we establish a regional disaster-system framework, DGR, which integrates Dynamics, Geology–meteorology cross-spatial coupling, and Risk phasing. Within this framework, we aim to capture the combined influence of endogenic tectonic forcing, exogenic hydrometeorological forcing, lithological erodibility, and human disturbance on hazard occurrence, and to provide a simplified conceptual mapping of the regional Earth system in tectonically active mountain terrain. Our results show that the disaster site was located in a runoff-incision-dominated reach characterized by disequilibrium between tectonic uplift and fluvial incision. On this basis, we propose the concept of a weak equilibrium window in the uplift–incision system, which may provide a useful geomorphic perspective for identifying potentially hazard-prone settings. Hydro-sedimentary analysis further suggests that the event was primarily flood-dominated, with sediment supplied mainly by proximal erosion rather than by sustained long-distance channel transport. Field-constrained reconstruction also indicates that engineering disturbance on the valley floor may have modified the natural transport corridor and amplified the interaction between human activity and natural hazard processes. More broadly, the results suggest that torrent disasters can serve as short-lived expressions of the long-term antagonism between internal and external geomorphic forcing. In this sense, the DGR framework provides a transferable conceptual and analytical approach for linking long-term uplift–incision evolution with short-term hazard response, and offers a practical basis for hazard identification and risk assessment in tectonically active mountain regions under climate change.

Keywords: Tectonic Uplift; Fluvial Incision; Earth System; Torrent; DGR Framework Model

https://doi.org/10.5194/egusphere-2026-2470
Preprint. Discussion started: 25 August 2026

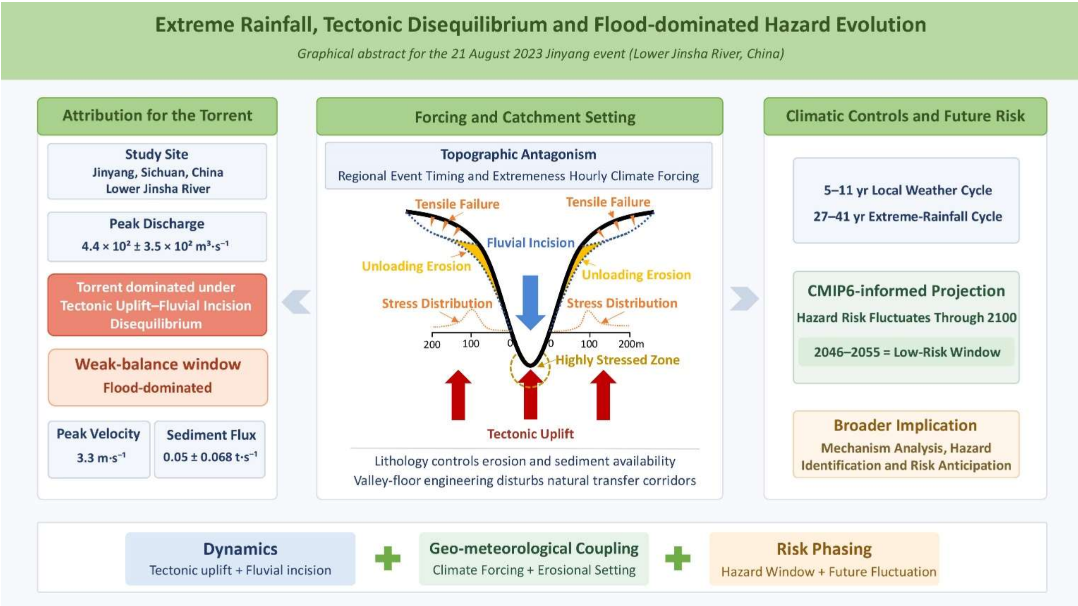

Graphical Abstract

1 Introduction

Anthropogenic warming has intensified the global hydrological cycle and heightened concern over climate-related hazards since the late twentieth century. By 2022, the global mean temperature had risen by 1.15°C relative to pre-industrial levels (1850–1900), and global surface warming is projected to exceed 1.5°C above pre-industrial levels within the next two decades (Zhou et al., 2021; Chen et al., 2022). Global warming increases atmospheric moisture-holding capacity, promotes the persistence of low-pressure systems, and weakens summer circulation, thereby contributing to prolonged heatwaves and droughts under high-pressure control, as well as more intense rainfall extremes under low-pressure dominance (Da Silva and Haerter, 2025). Studies further indicate that, for every 1°C of global warming, extreme precipitation intensity increases by approximately 7%—and by up to 15% in high-altitude regions—while rainfall variability rises by about 5% (Wen et al., 2022; Bi et al., 2023; Ombadi et al., 2023). Against this background, rainfall-induced landslides and torrent (In this study, "torrent" is used as an umbrella term for rapidly evolving, rainfall-triggered hazardous flow processes in steep mountainous catchments.) hazards have become increasingly frequent worldwide over the past two decades (Delchiaro et al., 2024). For example, in August 2010, Ladakh, India, experienced a heavy-rainfall-triggered flash flood that caused 234 fatalities and left more than 800 people missing (Gupta et al., 2012); on the following day, Zhouqu County, China, was struck by a

https://doi.org/10.5194/egusphere-2026-2470
Preprint. Discussion started: 25 August 2026

catastrophic debris flow that caused 1,557 fatalities and 208 missing persons. On a global scale, 206 torrent-related events were recorded in 2021 alone, accounting for 56.13% of all natural disasters and resulting in 4,393 fatalities and economic losses of USD 74.61 billion (Adrem et al., 2022). Data from the EM-DAT database further suggest that many of the most destructive events occur in mountainous regions, which are commonly tectonically active.

These observations raise a broader geomorphic question: does the increasing occurrence of extreme precipitation imply a strengthening of the antagonistic coupling between tectonic uplift and fluvial incision? If so, does this enhanced antagonism increase the likelihood of hazardous events, and are there diagnostic patterns that may support the early identification of potentially hazardous regions? More fundamentally, how can the spatiotemporal driving characteristics of the uplift–incision antagonism be quantified for comparable disaster events? In particular, a key challenge is to quantitatively characterize the feedbacks between the self-organizing evolution of catchment geomorphic units and torrent events in orogenic systems under the combined stresses of climate change and cumulative tectonic uplift.

The 21 August 2023 torrent event in the Lugaolin River Basin, Jinyang County, Sichuan Province, China, provides a representative case of hazard occurrence within a canyon system shaped by active tectonic uplift and fluvial incision (Times, 2023b; Times, 2023a). The event caused 6 fatalities, 46 missing persons and 21 injuries, with no remains recovered during the subsequent search. It also caused severe infrastructure damage and highlighted the amplified geomorphic response and uncertain hazard risk faced by orogenic belts under ongoing climate warming (Gu et al., 2025; Chen et al., 2025). This event therefore offers a valuable natural case for examining how tectonic forcing and climate-driven extremes jointly shape hazard processes. However, tectonic uplift acts as a long-term driver of landscape evolution over timescales of 10^4–10^5 years (Delchiaro et al., 2023), whereas torrent events triggered by extreme rainfall unfold over hours to days. At hazard locations, upward tectonic forcing and downward fluvial incision become focused within a single geomorphic setting, where they oppose one another. This local antagonism may reflect a more general pattern shared by similar hazards, with important implications for identifying comparable risk zones across broader spatiotemporal scales. A key unresolved question, therefore, is whether this uplift–incision antagonism at disaster sites is expressed in equilibrium or disequilibrium. If equilibrium prevails, does it correspond to greater hazard susceptibility? If disequilibrium dominates, which process outpaces the other—tectonic uplift or fluvial incision? And do sediment-transport characteristics differ systematically between these two states during hazardous events? Addressing these questions may help determine whether short-lived extreme events can be used to infer the coupled drivers and geomorphic responses of landscape evolution at broader scales.

To address these questions within an intrinsically coupled atmosphere–hydrosphere–lithosphere–human system (Moumeni et al., 2025), we integrate diverse data sources and quantitative metrics into a coupled technical framework—DGR, comprising Dynamics, Geology–Meteorology Cross-spatial Coupling, and Risk Phasing. This framework provides a simplified representation of the regional Earth system linking tectonic uplift, runoff incision, lithological heterogeneity and torrent hazards. Using the DGR framework, we quantify the spatial coupling among tectonic uplift, fluvial incision and lithological erodibility at the catchment scale, identify vertically and laterally differentiated zones of erosion and deposition, and reconstruct the hydrodynamic processes and sediment-transport behaviour associated with the catastrophic 21 August 2023

https://doi.org/10.5194/egusphere-2026-2470
Preprint. Discussion started: 25 August 2026

torrent event. In doing so, we provide a framework for linking geomorphic evolution on geological timescales with hazard response on meteorological timescales, thereby offering a basis for adaptive risk assessment of torrent hazards in tectonically active regions.

Unlike conventional hazard studies that focus primarily on rainfall forcing or local slope instability, the DGR framework seeks to reveal how long-term potential energy accumulated through tectonic uplift, fluvial incision and lithological resistance to erosion is instantaneously released under extreme rainfall conditions, and how these processes exert nonlinear controls on torrent activity within a unified spatiotemporal framework. This approach deepens our understanding of the role of individual disaster events in the phase transition of mountain-hazard risk and provides a scientific basis for risk management in tectonically active regions under ongoing climate warming.

https://doi.org/10.5194/egusphere-2026-2470
Preprint. Discussion started: 25 August 2026

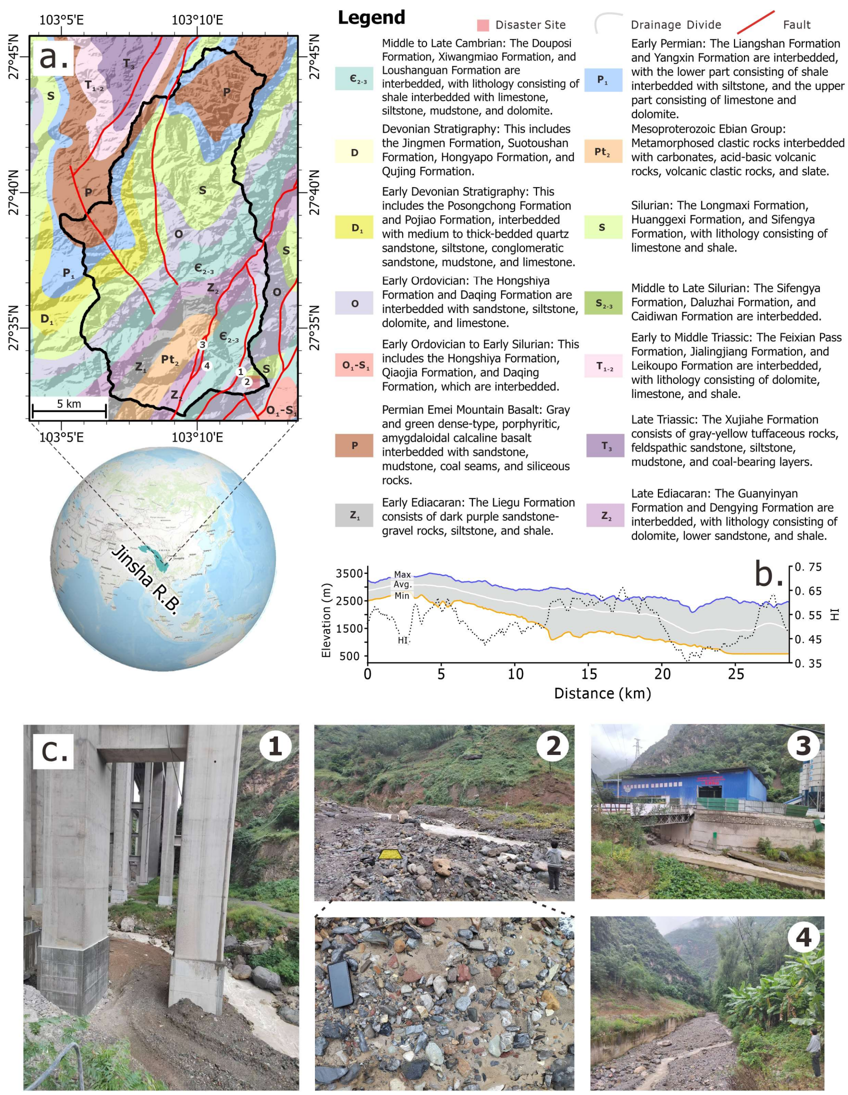

Fig. 1 Geological and Geomorphological Environment of the Lugaolin River Basin: Geological map (1:500,000); watershed elevation and erosional residual landforms (north–south); site photos (Oct 2025). HI (0–1) indicates residual erosion reflecting tectonic uplift and erosion interplay. Features: ① highway bridge piers in valley; ② coarse, angular riverbed rocks; ③ buildings on bank slope; ④ recent tributary supplying sediment.

https://doi.org/10.5194/egusphere-2026-2470
Preprint. Discussion started: 25 August 2026

2 Study Area

The study area is the Lugaolin River Basin, a tributary of the Jinsha River in southwestern China, covering 329.8 km². The basin is characterized by rugged mountainous terrain, with elevations ranging from 1,000 to 3,500 m. It is influenced by a subtropical monsoon climate, with mean annual precipitation of approximately 800 mm and interannual variability ranging from 601 to 1,152 mm. The population of the basin is about 35,000, with a population density of about 173 people per km². The 21 August 2023 torrent event occurred near the basin outlet (Fig. 1). The basin is underlain by Precambrian continental crust that formed and was subsequently reworked within the Yangtze Fold Belt during 1,000–800 Ma (Du et al., 2014), and regionally it lies within the carbonate platform of the southern Yangtze Block (Chen et al., 2024; Du et al., 2014). The tectonic evolution of the region can be broadly divided into four stages. During the basement formation stage (Z–Є), continental-margin rifting from the Mesoarchaean to Early Proterozoic (Zhang et al., 2023) established the structural framework for later Cambrian transgression and the development of shallow-marine shelf environments favourable for carbonate deposition. During the platform development stage (O–S), a carbonate platform formed under the warm-water conditions of low-latitude Ordovician–Silurian seas. During the differential reworking stage (D–P), Devonian rifting generated sedimentary basins, followed by Carboniferous–Permian marine transgressions that inundated much of the platform. During the final stage, Indosinian–Yanshanian orogenesis caused widespread thrust faulting and metamorphic reworking of the platform succession (Xu et al., 2025; Du et al., 2014; Yao et al., 2025).

3 Methodology

3.1 Research Design and Implementation

This study systematically investigates torrent hazards by constructing a multi-technology coupled framework for the multidimensional analysis of disaster characteristics (Fig. 2). First, river segments are classified into equilibrium and disequilibrium reaches in terms of uplift–fluvial incision antagonism on the basis of geomorphic dynamic parameters. This enables the quantification of spatial differentiation in erosion and sediment deposition during sediment transport, as well as the spatial variability of lithological resistance to erosion. Next, the SCS–CN hydrological model is used to reconstruct the spatiotemporal evolution of water–sediment processes triggered by extreme rainfall events. At the same time, the Revised Universal Soil Loss Equation (RUSLE) (Bekalo et al., 2025; Räsänen et al., 2024) is combined with limited sediment-flux records from hydrological stations to establish the relationship between surface connectivity and sediment transport rate, thereby constraining material supply. This approach provides a basis for exploring the coupling between hillslope material supply and channel sediment transport capacity under conditions of tectonic uplift. Building on these analyses, InSAR observations are used to compare changes in surface erosion-response zones before and after the disaster. In addition, the Standardized Precipitation Index (SPI), together with wavelet time–frequency analysis, is employed to identify the recurrence characteristics of historical extreme rainfall events. These characteristics are then combined with the Coupled

https://doi.org/10.5194/egusphere-2026-2470
Preprint. Discussion started: 25 August 2026

Model Intercomparison Project Phase 6 (CMIP6) SSP–RCP scenario database to explore potential future high-risk time windows and to assess the resilience of the hazard system.

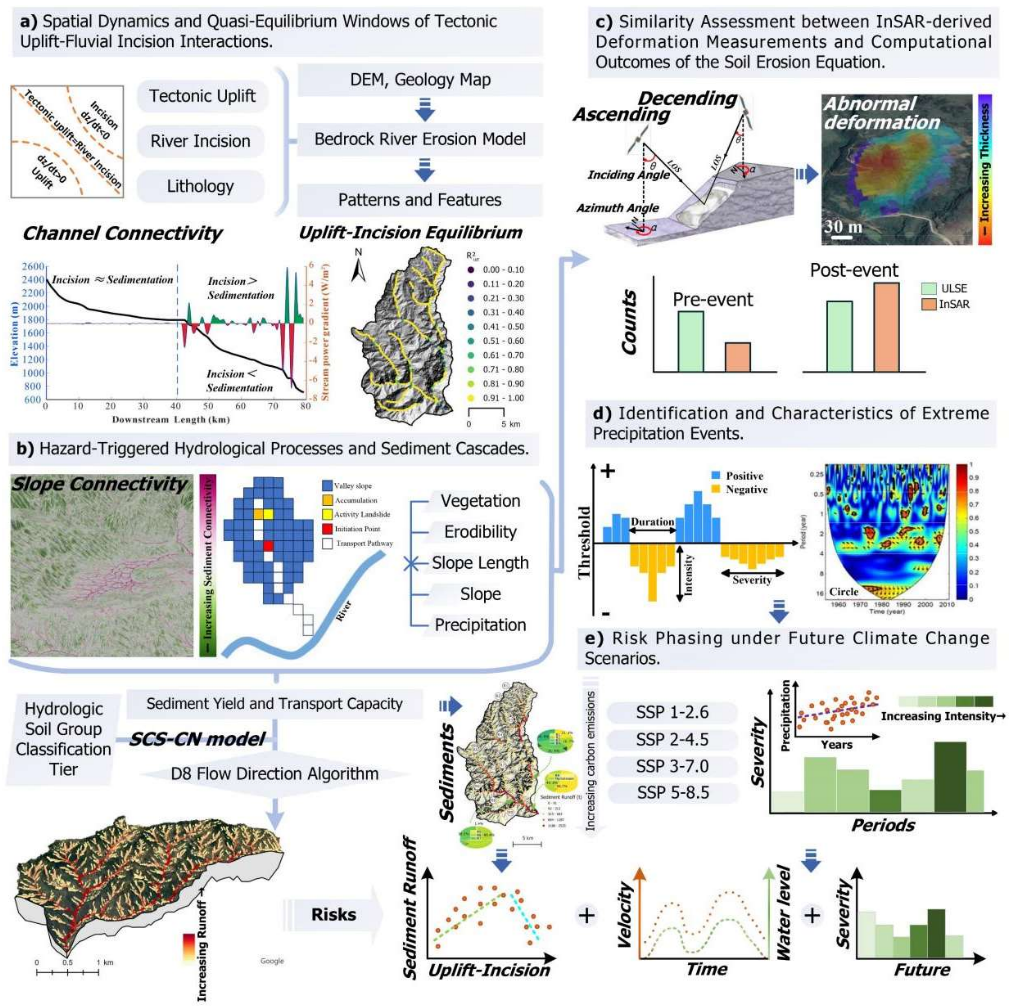

Fig. 2 Overview and Methodology

https://doi.org/10.5194/egusphere-2026-2470
Preprint. Discussion started: 25 August 2026

3.2 Data and Methods

3.2.1 Datasets and Preprocessing

This study integrates multiple datasets, including satellite imagery, hydrological observations, climate simulations, and soil-erosion-related data, to analyse and model the spatiotemporal dynamics of torrent events. The primary topographic dataset is a 2.5 m-resolution Digital Elevation Model (DEM) generated from the three-line stereo imaging system of the ZY-3 satellite and acquired on 27 May 2025. The DEM has a vertical error of ±3.8 m and is used to derive key geomorphic parameters, including the steepness index, catchment area, and slope, as well as to support terrain correction in InSAR-based ground-deformation analysis. The LS-factor dataset (DS-LS-GS1) was obtained from the National Tibetan Plateau / Third Pole Environment Data Center, with an error of less than ±1% (Sun et al., 2024b; Sun et al., 2023). This dataset is used to evaluate soil-erosion susceptibility and the spatial distribution of erosion potential. Sentinel-1A radar images and corresponding precise orbital data were also used, with a spatial resolution of 5 × 20 m. Ascending-track images were acquired between 10 January 2021 and 20 December 2021, whereas descending-track data span the period from 5 January 2021 to 15 December 2024. These data were used for InSAR-based ground-deformation monitoring. The VV polarization mode was selected because of its strong coherence, relatively low phase noise, and tolerance to long baselines. Atmospheric effects were corrected using GACOS (Generic Atmospheric Correction Online Service) data (Guo et al., 2024). For rainfall analysis, the ERA5-Land reanalysis dataset was used to identify the timing and regional extremeness of historical rainfall events. In this study, ERA5-Land serves as a spatially continuous regional climatic indicator rather than a source for point-scale reconstruction of local rainfall magnitude. In mountainous areas with limited ground-based monitoring, ERA5-Land provides hourly precipitation estimates with continuous spatial and temporal coverage and can reasonably represent regional-scale precipitation characteristics (https://cds.climate.copernicus.eu/). In addition, CMIP6 simulations for future rainfall from 2026 to 2100 were incorporated under four scenarios—SSP1-2.6, SSP2-4.5, SSP3-7.0, and SSP5-8.5—to assess potential future high-risk time windows under different carbon-emission pathways.

A 30 m-resolution spatial dataset of soil-erosion susceptibility was also used to estimate erosion rates, with a root mean square error of 0.0077 t·hr/(ha·MJ·mm) (Sun et al., 2024b; Sun et al., 2023), corresponding to approximately 22% of the regional mean value. NDVI (Normalized Difference Vegetation Index) data, obtained from China's National Scientific Data Center, were used to calculate vegetation cover, with a reported error of less than ±15% (Dong et al., 2021; Yang et al., 2019). In addition, long-term hydrological observations from the Qingkouatng, Doushaguang, Niujie, Ningnan, and Zhaojue stations were used to construct sediment transport functions for geographic units within the study area. Finally, a USDA curve-number grid dataset was used to support hydrological design, land-management applications, and groundwater-recharge modelling. This dataset represents runoff conditions derived from the European Space Agency global land-cover dataset for 2015 (ESA CCI-LC), resampled to 250 m and georegistered with the global hydrologic soil group product HYSOGs 250 m (Jaafar et al., 2019). Collectively, these datasets provide the basis for analysing the dynamic interactions among tectonic uplift, fluvial incision, and extreme rainfall in torrent hazards.

https://doi.org/10.5194/egusphere-2026-2470
Preprint. Discussion started: 25 August 2026

3.2.2 Core Methods

(1) Tectonic Uplift and Fluvial Incision Equilibrium

Firstly, Steepness Index and Lithological Correction

When the longitudinal profile of a river is in a state of tectonic uplift-fluvial incision equilibrium (i.e., the uplift rate equals the incision rate), the steepness index is used to reflect the relative rate of tectonic uplift (Demoulin et al., 2017; Snyder et al., 2000; Kirby and Whipple, 2001). An integration method provides more accurate steepness index values (Su et al., 2019; Perron and Royden, 2013), where the slope of the χ-z curve is obtained, expressed as:

$$\chi=\int_0^x \left(\frac{A_0}{A(x')}\right)^{m/n} dx', \quad z=\left(\frac{E}{KA_0^m}\right)^{1/n}\chi \qquad (1)$$

Here, when the reference area (A_0) is 1 m², the slope of the first fitting function of the χ-z plot is taken as the steepness index (Perron and Royden, 2013; Moumeni et al., 2025). Further, we define the linear fitting coefficient $R^2_{U/E}$ as the balance coefficient of tectonic uplift and fluvial incision equilibrium, where a value closer to 1 indicates a more balanced state between uplift and incision. Typically, a reference concavity value (θ = 0.45) is used to obtain a normalized steepness index (k_{sn}) to compare relative differences in uplift rates (Wang et al., 2017; Zhang et al., 2018). However, the steepness index still reflects lithological influences on the uplift rate ($k_{sn}=U_e$, where U_e is the uplift rate in mm/yr and e is the lithological factor). To eliminate errors from heterogeneous lithology, a correction is applied to isolate the relative characteristics of uplift rates by using the following formula:

$$\tilde{k}_{sn}=\frac{\hat{k}_{sn_{k,i}}}{\bar{k}_{sn_k}}\times\bar{K}_{sn} \qquad (2)$$

In this equation, $\hat{k}_{sn_{k,i}}$ is the normalized steepness index at location i within a specific lithological zone k of the riverbed ($m^{0.9}$, where m is a constant influenced by precipitation, lithology, and other factors), $\bar{K}_{sn}$ is the mean normalized steepness index of all lithological units in the study area, and $\bar{k}_{sn_k}$ is the average normalized steepness index within lithological zone k ($m^{0.9}$) (Gu et al., 2023; Shi and Shao, 2014). Since bedrock erodibility within the same lithological zone is highly homogeneous, the ratio $\hat{k}_{sn_{k,i}}/\bar{k}_{sn_i}$ can effectively minimize the lithological influence (e), yielding a corrected $\tilde{k}_{sn}$ that reflects the relative uplift rate after error correction. The term $\bar{K}_{sn}/\bar{k}_{sn_k}$ reflects the relative erodibility of different bedrock units in the region. The correction principle is as follows: if a specific lithological group is harder than the regional lithological average, the measured k_{sn} value will be higher compared to the ideal condition of homogeneous lithology. In this case, $\bar{K}_{sn}/\bar{k}_{sn_k}<1$ and multiplying with k_{sn} compensates for the influence of lithology. Conversely, if a lithological group is more erodible, the measured k_{sn} value will be lower than the idealized homogeneous lithology condition and multiplying with k_{sn} when $\bar{K}_{sn}/\bar{k}_{sn_k}>1$ compensates for its erodibility.

Secondly, Stream Power and Its Gradient

Stream power (Ω, W/m) represents the rate at which runoff's gravitational potential energy is converted into kinetic energy, defined as:

$$\Omega = \gamma \cdot Q \cdot s \quad (3)$$

where γ is the unit weight of water (9800 N/m³), Q is the discharge (m³/s), and s is the slope of the water surface, which is approximately the riverbed gradient (Pérez-Peña et al., 2010). The runoff volume can be expressed as:

$$Q = aA^b \quad (4)$$

where A is the upstream catchment area (m²), and a and b are fixed coefficients that depend on climate, geology, and topographic conditions. The stream power gradient (ω, W/m²) is defined as:

$$\omega = \Delta\Omega / \Delta w \text{ or } \omega = \Delta\Omega / \Delta L \quad (5)$$

where ΔΩ, Δw, and ΔL are the changes in stream power, river width, and river length, respectively, between two points. In mountainous areas where downcutting erosion is more active, the formula $\omega = \Delta\Omega / \Delta L$ is used to describe erosion and sedimentation. When $\omega > 0$, riverbeds are eroded; when $\omega < 0$, sedimentation occurs; and when $\omega = 0$, transport or erosion equals sedimentation (Gu et al., 2021; Gu et al., 2019).

(2) SCS-CN Model, Flow Velocity, and Uncertainty Analysis

Firstly, SCS-CN Model and Flow Velocity

In regions where continuous, high-precision runoff data is unavailable, it is challenging to support the boundary conditions and calibration data required for distributed hydrological models. In contrast, the SCS-CN model, due to its simple structure, can estimate flow rates with fewer parameters and exhibits strong robustness, making it more suitable for areas without observational records and for small to medium-sized watersheds (Wang et al., 2025; Mockus, 1964; Soulis and Valiantzas, 2012). The SCS-CN model is based on the water balance equation and two fundamental assumptions: rainfall (P) can be expressed as the sum of initial abstraction (I_a), runoff (Q), and infiltration (F), with the actual infiltration (F) to the potential maximum retention (S) ratio reflecting the actual runoff (Q) to the maximum possible runoff (P - I_a) ratio. Furthermore, S and I_a are directly proportional, as shown in the following equations:

$$P = I_a + F + Q \quad (6)$$

$$\frac{Q}{P - I_a} = \frac{F}{S} \quad (7)$$

$$I_a = \lambda S \quad (8)$$

The equation for runoff generation based on numerous runoff-conversion experiments has been widely accepted, with the initial abstraction coefficient (λ) typically assumed to be 0.2 (Mockus, 1964; Wang et al., 2025):

$$Q_p = \begin{cases} 0 & (P \leq \lambda S) \\ \frac{(P - \lambda S)^2}{(P - I_a + S)} & (P > \lambda S) \end{cases} \quad (9)$$

Where P represents precipitation (mm), F is cumulative infiltration (mm), excluding initial abstraction (I_a), Q represents the runoff depth generated by each rainfall event (mm), and S is the maximum potential surface retention (mm), defined as:

$$S = \frac{25400}{CN} - 254 \quad (10)$$

Where CN refers to the USDA curve number, which reflects the combined hydrological characteristics of the surface, with higher values (ranging from 0 to 100) indicating stronger runoff potential. Based on the estimated runoff, we use the D8

https://doi.org/10.5194/egusphere-2026-2470
Preprint. Discussion started: 25 August 2026

algorithm (Yang et al., 2023) to convert precipitation into flow values every 2 hours. The maximum (CN_{max} = 4) and minimum (CN_{min} = 3) CN values in the study area provide the uncertainty range for the flow values. The calculation for flow velocity is as follows:

$$v(t)=\frac{Q(t)}{A(t)} \quad (11)$$

$$Q=\frac{1}{n}AR^{2/3}S^{1/2} \quad (12)$$

$$A=\sum_{i=1}^{n-1}\left(\frac{\max(0,h+z_{\min}-z_i)+\max(0,h+z_{\min}-z_{i+1})}{2}\right)(x_{i+1}-x_i) \quad (13)$$

$$R=\frac{\sum_{i=1}^{n-1}\sqrt{(x_{i+1}-x_i)^2+(z_{i+1}-z_i)^2}}{A} \quad (14)$$

where Q is the runoff (m³/s), n is the Manning roughness coefficient (Yang et al., 2023; Wei et al., 2024), A is the cross-sectional area of flow (m²), R is the hydraulic radius (m), S is the valley slope, x_i is the distance from the ith point to the end of the river cross-section, and z_i is the corresponding elevation. The time, t, is in seconds.

Secondly, Sediment Yield and Sediment Transport Rate

The material sources for rivers and torrent primarily originate from slope erosion and landslide deposition, which can be estimated using the Universal Soil Loss Equation (USLE). The material supply (E_i) is calculated as:

$$E_i=R_i\cdot K_i\cdot L_i\cdot S_i\cdot C_i\cdot P_i \quad (15)$$

where E_i is the total erosion (t), R_i is the rainfall erosivity (MJ·mm·hm⁻²·h⁻¹·year⁻¹), K_i is the erodibility factor (t·hr/(ha·MJ·mm)), L_i is the slope length (m), S_i is the slope, C_i is the vegetation cover, and P_i is the conservation practice factor (Sun et al., 2024a).The sediment delivery ratio (SDR) can be calculated using the Index of Conductivity (IC) as:

$$SDR_i=\frac{SDR_{max}}{1+e^{\frac{IC_0-IC_i}{k}}} \quad (16)$$

where SDR_{max} is the maximum theoretical value, IC_0 and k are calibration parameters defining the SDR-IC relationship (Vigiak et al., 2012; Räsänen et al., 2024). IC is defined as:

$$IC=\log_{10}(D_{up}/D_{dn}) \quad (17)$$

where D_{up} reflects the potential for material source transport from an upstream area to the downhill, and D_{dn} reflects the distance from the debris to the nearest confluence point (Borselli et al., 2008). The parameter IC_0 determines the "transportability," with higher values indicating more pixels classified into the low SDR zone, leading to a decrease in total flux and peak values. The slope parameter k defines the "concentration" of the flux, with lower values resulting in a steeper SDR-IC curve, causing the model to approach a binary classification (transport or no transport). Increasing k will expand the range of material supply. The IC-SDR model effectively reflects the connectivity gradient between slope, valley, and river systems, distinguishing high-connectivity transport channels from sedimentation-retention units. Thus, the total sediment transport rate (t/s) for the watershed area is expressed as:

$$E=\sum_{i=1}^{n}E_i\cdot SDR_i \quad (18)$$

https://doi.org/10.5194/egusphere-2026-2470
Preprint. Discussion started: 25 August 2026

Due to the difficulty in determining IC_0 and k, we estimate the observed SDR (SDR_{obs} = 0.8 ± 0.7) based on sediment output records from multiple neighboring hydrological stations.

Thirdly, Uncertainty Estimation

To estimate the uncertainty in the flow and sediment transport rate calculations, we use the linear propagation principle:

$$\sigma_Y=\sqrt{\sum_{i=1}^{n}\left(\frac{\partial Y}{\partial X_i}\cdot\sigma_{X_i}\right)^2} \tag{19}$$

Where σ_Y is the standard deviation of the output result Y, $\frac{\partial Y}{\partial X_i}$ is the partial derivative of the model with respect to the input parameter X_i (sensitivity), and σ_{X_i} is the standard deviation of the input parameter X_i (Liu and Gupta, 2007; Fienen et al., 2010).

(3) InSAR Observation of Surface Erosion and Deformation Response

Sediment transport originates from surface erosion, leading to surface deformation. The use of SBAS-InSAR (Li et al., 2025) enables the detection of surface deformation patterns in the study area before and after the occurrence of the disaster. This method is a high-precision surface deformation monitoring technique that allows for long-term tracking of surface changes. By processing multiple microwave interferometric images through steps such as removing topographic, atmospheric, and flat-earth phases, and applying filtering techniques, the line-of-sight deformation rate can be obtained (Cai et al., 2023). We perform a three-dimensional decomposition of the two average deformation rate maps based on ascending and descending SAR images to extract vertical deformation rates. The deformation zones are then identified using the "Cluster and Spatial Outlier" tool in the ArcGIS software platform. This approach provides a robust means to analyze and visualize the spatial distribution of surface deformations, offering valuable insights into the impact of erosion and sediment transport on the region's geomorphology.

(4) Identification of Extreme Rainfall Events and Return Period Analysis

Extreme weather events include both extreme rainfall and extreme droughts. The run theory, through threshold-based identification, characterizes the "duration," "intensity," and "severity" of extreme rainfall events, making it particularly suitable for analyzing such extreme weather occurrences (Huang et al., 2021; Yevjevich, 1969). Before identifying the characteristics of extreme rainfall events, the Gamma probability function is used to convert rainfall data into the Standardized Precipitation Index (SPI), which eliminates regional bias in precipitation data, facilitating cross-regional comparisons. The probability density function of the Gamma distribution is given by:

$$g(x)=\frac{1}{\beta^{\alpha}\Gamma(\alpha)}x^{\alpha-1}e^{-x/\beta} \tag{20}$$

where x represents precipitation (mm), α is the shape parameter that controls the distribution curve's shape, β is the scale parameter that determines the dispersion of values, and Γ(α) is the Gamma function. This function's domain and distribution closely match the actual distribution of precipitation events, which generally exhibit a high frequency of low values and a small number of extreme high values (Edwards, 1997). The cumulative distribution function (CDF) of the Gamma distribution is:

https://doi.org/10.5194/egusphere-2026-2470
Preprint. Discussion started: 25 August 2026

$$G(x) = \frac{1}{\Gamma(\alpha)} \int_0^x t^{\alpha-1} e^{-t} \; dt \qquad (21)$$

where $t = \frac{x}{\beta}$. To handle cases where $x = 0$, which is undefined for the Gamma distribution, a zero-function correction is introduced:

$$H(x) = q + (1 - q)G(x) \qquad (22)$$

where q is the probability of no precipitation. By applying an inverse normal transformation to $H(x)$, we obtain the SPI:

$$SPI = \phi^{-1}(H(x)) \qquad (23)$$

The severity of precipitation can be described as the total of the SPI values across the duration of multiple extreme rainfall events:

$$S_{ij} = \left(\frac{1}{m} \sum_{i=1}^{m} |\, SPI_i \,|\right)_j \qquad (24)$$

where m is the number of extreme wetting events, representing precipitation-dominated wetting occurrences (Farahmand and Aghakouchak, 2015). The maximum SPI during the duration of the event represents the intensity of the extreme rainfall. For identifying extreme rainfall cycles, the wavelet power spectrum is used as an analytical tool. Wavelet coefficients are employed to reflect the energy distribution of extreme rainfall events across different time and frequency scales, thus capturing the time-varying characteristics of non-stationary signals.

4 Results

4.1 Spatial distribution of the antagonism between tectonic uplift and fluvial incision

Using the lithology-corrected steepness index (k_{sn}) and steady-state coefficient ($R^2_{\mathrm{U/E}}$), we characterized the spatial pattern of the antagonism between tectonic uplift and fluvial incision (Figs. 3 and 4) and quantified bedrock resistance to erosion across the catchment (Fig. 5). The upstream tributaries R1–R3 are associated with relatively low k_{sn} values, indicating comparatively gentle and balanced tectonic uplift. By contrast, the downstream tributaries R7–R9 exhibit markedly higher k_{sn} values, reflecting stronger tectonic forcing. At the same time, $R^2_{\mathrm{U/E}}$ varies alternately along the longitudinal valley profile (Fig. 3b). Based on the significance threshold of the linear correlation coefficient, we define $R^2_{\mathrm{U/E}}$=0.31 as the key threshold for identifying a weak equilibrium window (Notes: χ-z linear correlation coefficient $R_{\mathrm{U/E}}=r_{\alpha=0.05}$; The threshold values used in this study, including the weak-equilibrium threshold of $R^2_{\mathrm{U/E}}$ and the apparent transition k_{sn}, are data-constrained for this case study. They should therefore be interpreted as empirically derived reference values rather than universally transferable geomorphic thresholds). When $R^2_{\mathrm{U/E}}$>0.31, the system is regarded as relatively balanced, whereas $R^2_{\mathrm{U/E}}$<0.31 indicates disequilibrium. At the scale of the entire catchment, Fig. 3c shows only a weak relationship between $R^2_{\mathrm{U/E}}$ and k_{sn} ($R_{\mathrm{U/E}}$= 0.14<$r_{\alpha=0.05}$), suggesting that uplift rate alone contributes little to the establishment or loss of steady state. This implies that another component of the antagonistic system—namely fluvial incision—plays the more important role. In contrast, a significant correlation exists between $R^2_{\mathrm{U/E}}$ and elevation ($R^2_{\mathrm{U/E}}$>$r_{\alpha=0.05}$=0.26), indicating that the spatial trend in steady state

https://doi.org/10.5194/egusphere-2026-2470
Preprint. Discussion started: 25 August 2026

is strongly linked to the cumulative effect of tectonic uplift, expressed here by topographic elevation. In general, higher elevations tend to correspond to a more balanced relationship between tectonic uplift and fluvial incision.

Within the valley system, disequilibrium channel segments alternate predominantly between tectonic-dominated and incision-dominated reaches (Fig. 3d). In disequilibrium reaches dominated by tectonic forcing, uplift steepens the channel power gradient and promotes fluvial incision. By contrast, in reaches dominated by incision, energy-dissipation feedback emerges, characterized by a sequence of sedimentation → channel-gradient reduction → weakening of incision intensity (Figs. 3d and 4). Stream power and its gradient further illustrate the spatial dynamics of incision and deposition (Figs. 4a–e). As shown in Fig. 4a, high stream-power values are concentrated in steep channel reaches. Figures 4b–e quantify the stream-power gradient and reveal an alternating spatial pattern of downcutting and depositional segments. Pixel-based statistics (Fig. 4d) show that downcutting reaches account for 72% of the total channel length and are concentrated in sections with marked longitudinal elevation change, whereas depositional reaches account for only 28%. This pattern highlights the strong geomorphic feedback between hydraulic forcing and tectonic setting. In reaches with high stream-power gradients, fluvial incision deepens the riverbed and steepens adjacent valley-side slopes, thereby increasing local instability. Continued downcutting can promote slope failure, landslide deposition, and channel infilling. By contrast, depositional reaches are characterized by lower flow velocity and the deposition of coarse debris, which suppresses the self-amplifying effect of downcutting and promotes energy dissipation. The disaster occurred in such a dissipative setting, showing a clear tendency for incision to outpace tectonic uplift (Fig. 3).

https://doi.org/10.5194/egusphere-2026-2470
Preprint. Discussion started: 25 August 2026

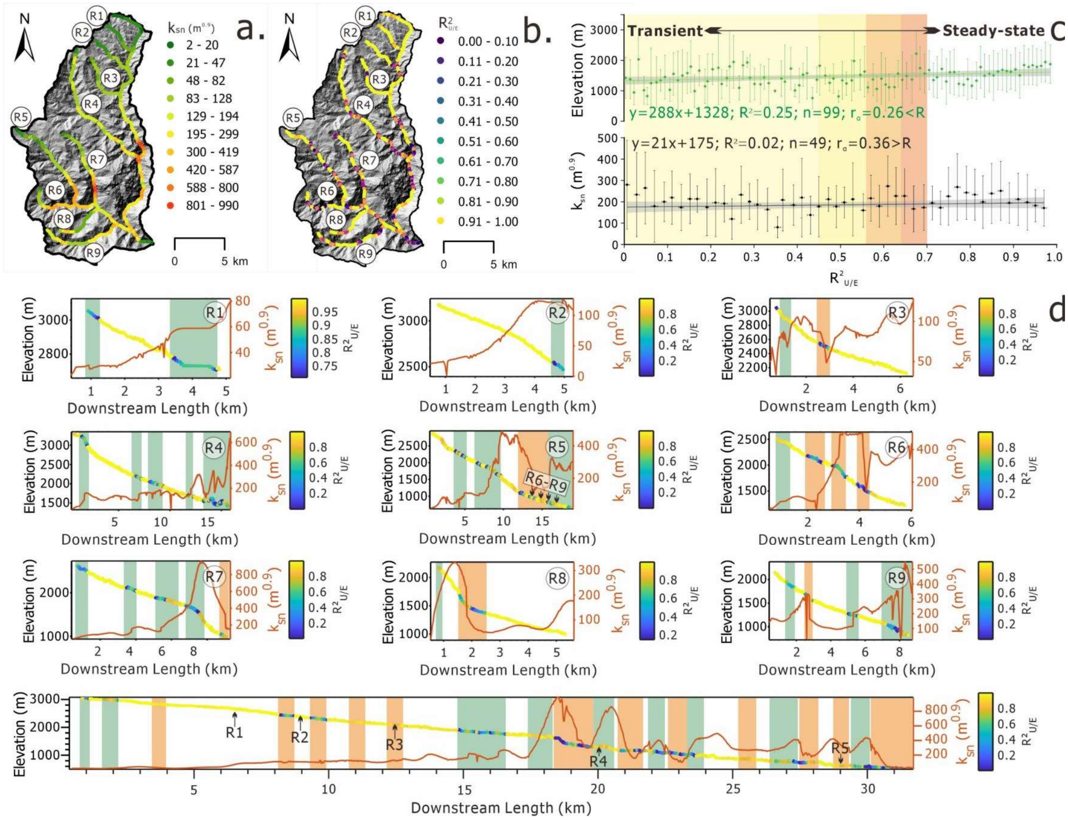

Fig. 3 Tectonic Uplift-Fluvial Incision Weak Equilibrium Window: ***a***, Spatial characteristics of the steepness index and steady-state coefficient in the main stream channel.; ***b***, Variation of elevation and steepness index with the steady-state coefficient; ***c***, Changes in steepness index and elevation with the steady-state coefficient (Notes: Background color deepens from light yellow to the right, with significance levels α of 0.01, 0.001, 0.0001, and 0.00001, respectively); ***d***, Transient segments of the main stream channel (Notes: gray-green background indicates segments where tectonic uplift rate>fluvial incision rate, while orange background indicates segments where fluvial incision>tectonic uplift. For disequilibrium segments, a decrease in the $\tilde{k}_{sn}$ value downstream indicates tectonic uplift shaping, whereas an increase downstream indicates fluvial incision shaping).

330

https://doi.org/10.5194/egusphere-2026-2470
Preprint. Discussion started: 25 August 2026

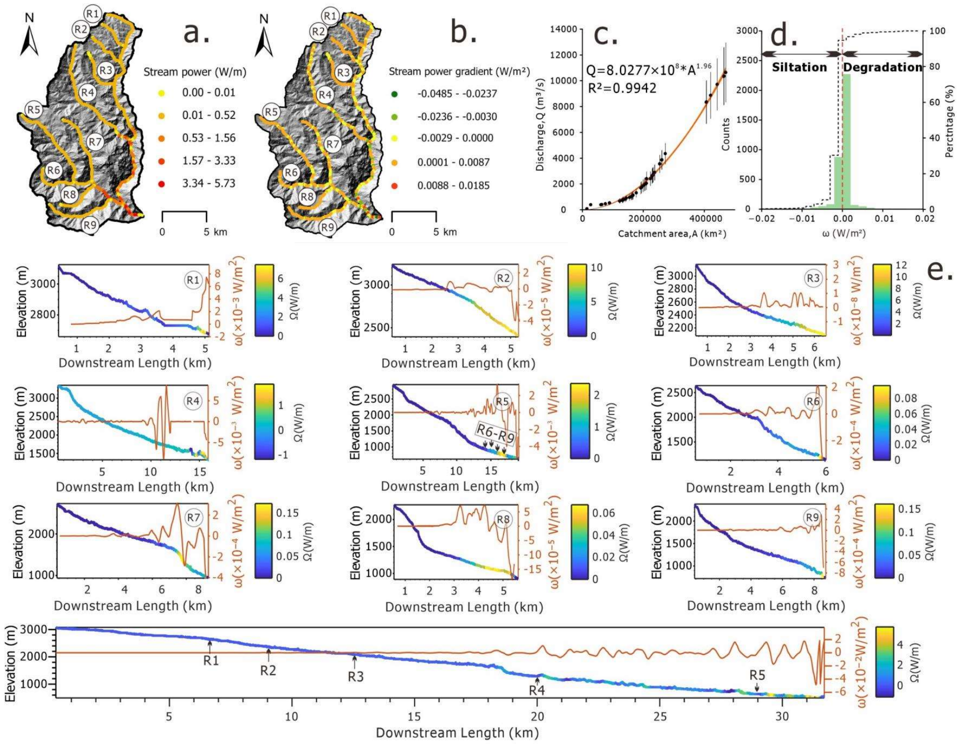

Fig. 4 Stream Power and its Gradient Changes on a Multi-Year Scale: a, Stream power; **b,** Stream power gradient; **c,** Relationship between watershed area and Runoff on a multi-year scale; **d,** Distribution of Stream power gradient values; **e,** Externally driven characteristics along the longitudinal profiles (Notes: ω＜0 represents sedimentation, and ω>0 represents incision).

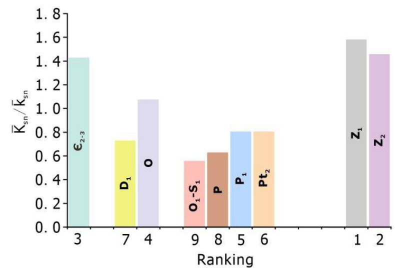

Fig. 5 Erosion Susceptibility Characteristics of Bedrock Riverbeds (Notes: The smaller the value on the vertical axis, the stronger the lithological resistance to erosion; The lithology legend is consistent with that in Fig. 1).

https://doi.org/10.5194/egusphere-2026-2470
Preprint. Discussion started: 25 August 2026

4.2 Spatiotemporal patterns of runoff, flow velocity and sediment transport

By reconstructing the spatiotemporal distributions of runoff, flow velocity and sediment transport rate in disaster-prone channel reaches (Fig. 6), we captured the hydrodynamic evolution of the 19–21 August 2023 torrent event (UTC). These results provide a multidimensional view of the event's hydraulic conditions. Figure 6 shows the distribution of runoff across the channel network at different times. Between 04:00 and 06:00 on 19 August, the main channel network was dominated by baseflow, with discharge generally below 0.3 m^3/s (Fig. 6a). By midnight on the same day (Fig. 6b), substantial upstream confluence caused discharge at the basin outlet to exceed $4\times10^2 \pm 3.5\times10^2$ m^3/s. In the early hours of 20 August (Fig. 6c), runoff receded and remained relatively stable for about six hours, with most tributaries maintaining discharge near 0.24 m^3/s. By 22:00 on 20 August (Fig. 6d), a second rainfall pulse triggered renewed confluence, with extreme discharge values exceeding $4.4\times10^2 \pm 3.5\times10^2$ m^3/s, extending into the middle and lower reaches of the basin. Between 02:00 and 04:00 on 21 August (Fig. 6e), flow stabilized at approximately 1 m^3/s, marking the waning stage of the event.

Topographically, the valley drops steeply from the headwaters to the disaster reach near the basin outlet. A flood-retention zone is developed at an elevation of approximately 600 m between cross-section A–B, where the local valley gradient is 6.8% ± 6.3%. This reach functions both as a depositional zone and as a key zone of energy conversion during flood peaks. Estimates based on different Manning roughness scenarios reveal substantial variation in flow velocity. For a natural rocky channel (n = 0.02–0.025) transitioning to a coarse gravel-bed channel (n=0.035–0.045), peak flow velocity decreases by 55%, while water level rises by approximately 0.47 m. Under an extremely obstructed-bed scenario, characterized by large boulders and dense vegetation (n=0.15–0.20), mean water level increases by about 1.3 m (Figs. 6i and 6j).

At the same time, Fig. 6g shows the temporal evolution of discharge and sediment concentration in the disaster-prone reach, indicating that the event was flood-dominated rather than debris-flow-dominated. The peak sediment transport rate reached 0.05 ± 0.068 t/s, and a clear lag occurred between the sediment peak and the discharge peak. Sediment transport began to increase approximately 2–4 hours before the sharp rise in discharge (Fig. 6g). This lag probably reflects the early entrainment of loose surface material by initial runoff, followed by progressively stronger hydraulic control on sediment transport as runoff intensified. Figure 7 further illustrates the spatial variation in sediment transport rate at a 2-hour interval. Unlike runoff, sediment generated within the basin does not accumulate continuously downstream, but is instead transported intermittently, with a considerable proportion deposited along the transport pathway. Sediment flux in the disaster reach is derived mainly from nearby hillslope erosion and from right-bank tributaries (R5–R9) (Fig. 7h), whereas sediment contributions from left-bank tributaries (R1–R4) are limited.

https://doi.org/10.5194/egusphere-2026-2470
Preprint. Discussion started: 25 August 2026

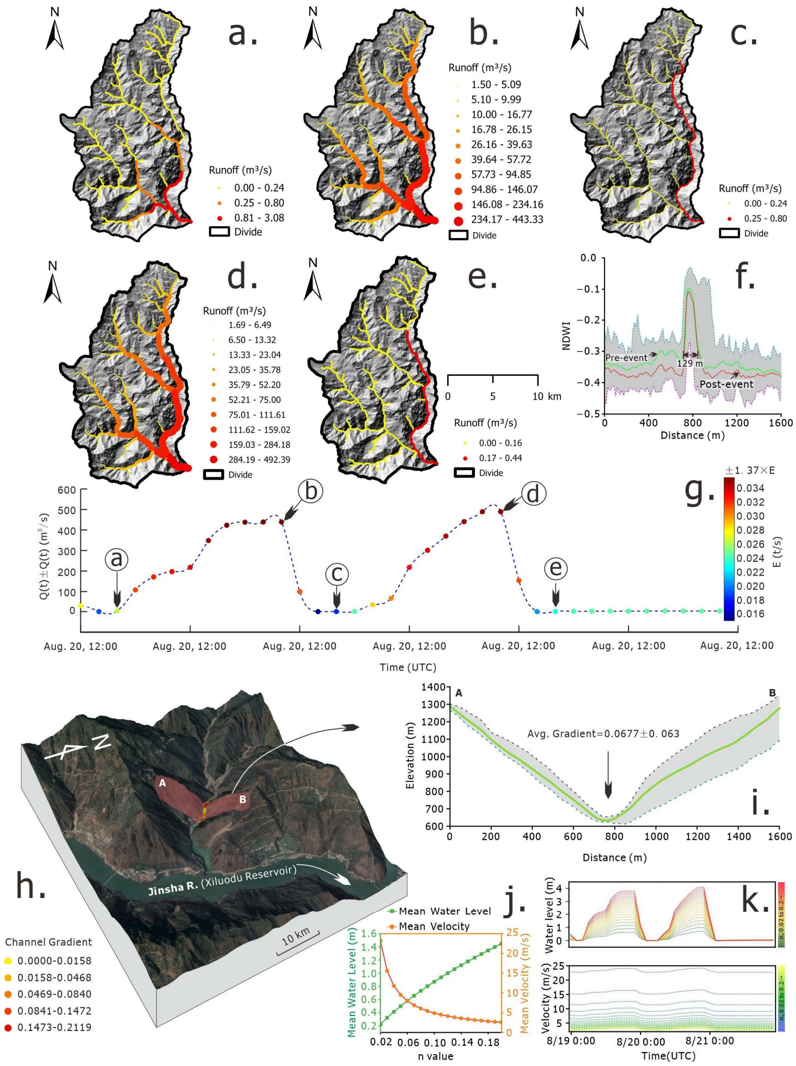

Fig. 6 Changes in Flow and Velocity During the Flood-debris flow: a, 4:00–6:00 AM, August 19, 2023; **b,** 10:00–12:00 PM, August 19, 2023; **c,** 4:00–6:00 AM, August 20, 2023; **d,** 10:00–12:00 PM, August 20, 2023; **e,** 2:00–4:00 AM, August 21, 2023; **f,** Remote sensing humidity index (NDWI); **g,** Changes in Runoff and sediment transport rate at the disaster location; **h,** Stream power gradient at the disaster section; **i,** Cross-section of the disaster valley; **j,** Variation of average water level and flow velocity with Manning's Roughness Coefficient; **k,** Water level and flow velocity in different Manning's roughness coefficients.

https://doi.org/10.5194/egusphere-2026-2470
Preprint. Discussion started: 25 August 2026

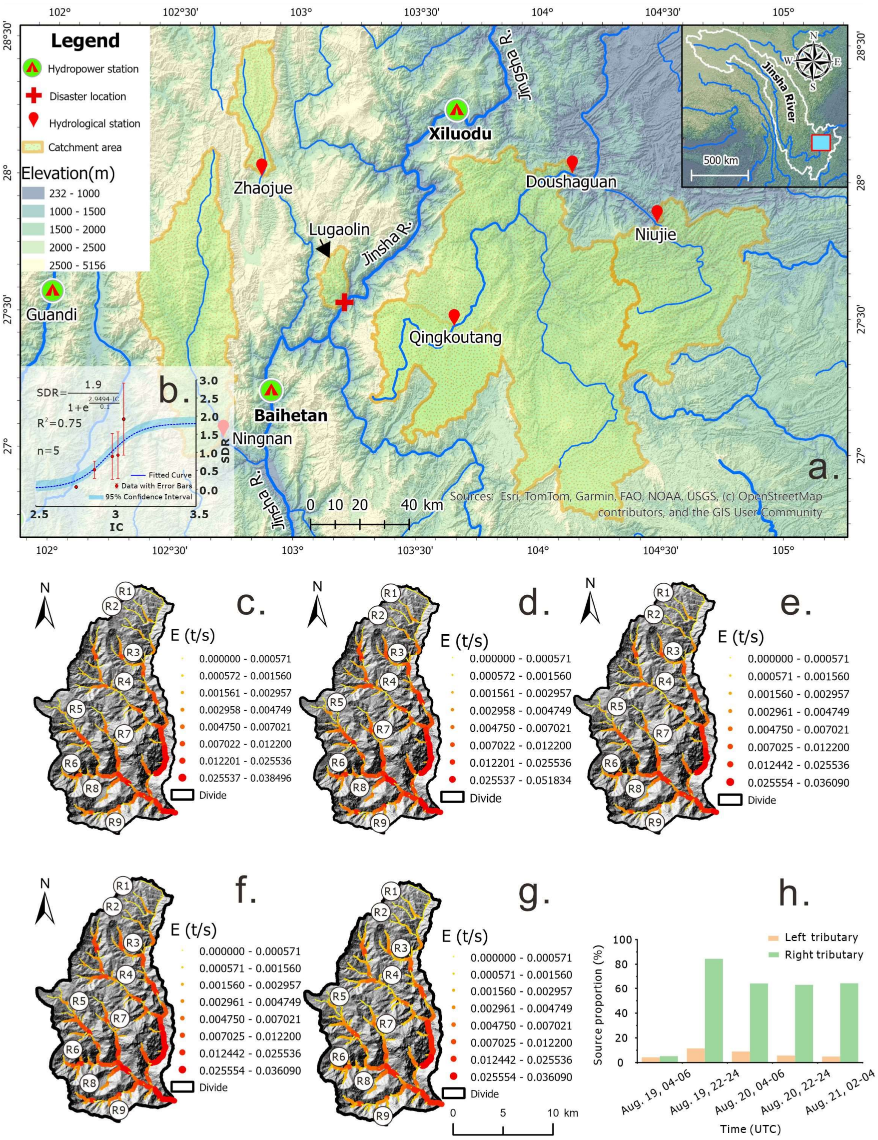

Fig. 7 Sediment Transport Rate Fitting Characteristics and Sediment Flux at Different Time Intervals: Hydrological stations distribution; IC-SDR fit for watershed connectivity vs. sediment transport; sediment fluxes: 4–6 AM and 10 PM–12 AM on Aug 19–21, 2023; proportional sediment source contributions from left and right at disaster site.

4.3 Surface deformation responses after the disaster

By comparing the spatial distributions of vertical and along-slope deformation rates before and after the extreme rainfall event of 21 August 2023 in Jinyang County, Fig. 8 reveals the strong influence of high-intensity rainfall on the stability of steep canyon slopes. Before the rainfall event, deformation rates were relatively low and spatially stable, with values concentrated between 50 and 0.02 mm/yr, and an average of 34 mm/yr. Deformation was particularly limited in high-elevation areas. After the extreme rainfall, however, deformation became much more spatially dispersed, and the area affected by deformation rates exceeding 330 mm/yr expanded markedly. The mean deformation rate increased to 96 mm/yr, indicating an almost threefold increase in slope-deformation intensity.

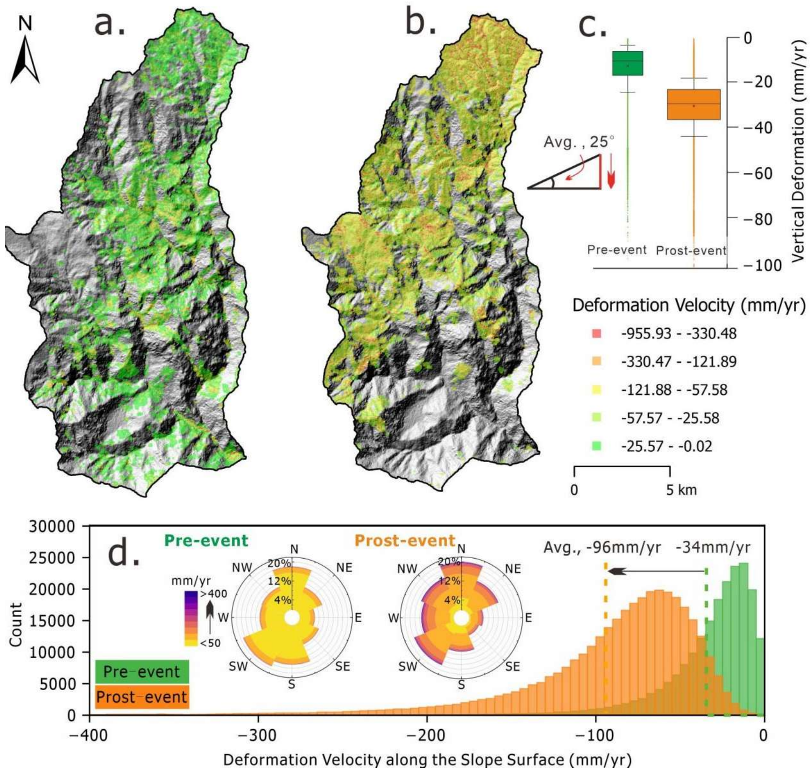

Fig. 8 Comparison of Surface Anomalous Deformation Characteristics Before and After the Extreme Precipitation Event: a, Average surface anomalous deformation speed along the slope from August 2022 to July 2023; **b,** Surface anomalous deformation speed along the slope from September 2023 to August 2024; **c,** Vertical deformation rate in anomalous deformation areas; **d,** Deformation rate along different slope orientations.

https://doi.org/10.5194/egusphere-2026-2470
Preprint. Discussion started: 25 August 2026

Figure 8c compares vertical deformation rates and highlights pronounced changes in steep-slope areas. The median deformation rate increased from 12.4 mm/yr to 38.7 mm/yr, and the number of outliers also rose noticeably, suggesting an enhanced likelihood of more aggressive slope processes such as land-sliding. When deformation was analyzed by slope aspect, the overall frequency distribution did not change fundamentally before and after the rainfall event, although moderate shifts were observed. Specifically, deformation frequency decreased on east-facing (−0.56%), southeast-facing (−4.3%), south-facing (−5.8%) and southwest-facing (−1.1%) slopes, but increased on north-facing (+1.8%), northeast-facing (+2.8%), west-facing (+3.0%) and northwest-facing (+4.2%) slopes. This pattern suggests that deformation became more frequent on relatively shady slopes after the rainfall event. Such slopes typically receive less solar radiation, maintain lower mean temperatures and higher humidity, and therefore favour prolonged moisture retention. Following intense rainfall, these conditions promote the softening of soil and weathered material, thereby increasing susceptibility to deformation. Overall, the results indicate that extreme rainfall may accelerate erosion and instability on shady slopes through hydrological erosion and soil softening.

4.4 Historical extreme rainfall and recurrence characteristics

The spatiotemporal distribution and periodic variability of extreme rainfall provide important insights into the behaviour of the regional climate system. Figure 9 summarizes the temporal patterns of extreme rainfall in the study area in terms of timing, intensity, severity and periodicity. Figure 9a shows the occurrence time, intensity and severity of historical extreme rainfall events, whereas Figs. 9b and 9c present the wavelet power spectra of rainfall intensity and severity in time–frequency space. At a timescale of approximately 2,000 days (5–6 years), rainfall severity fluctuates markedly, with high-severity years occurring in 1997 and 2022 and relatively low-severity years in 2007 and 2012. As the timescale increases, rainfall severity becomes more stable overall, although several pronounced peaks and troughs remain, including peaks at approximately 11,000 days (~30 years) and 15,000 days (~41 years). This suggests that the region is influenced by multiple superimposed cycles of extreme rainfall variability. According to the global wavelet spectrum, these fluctuation periods exceed the significance threshold (red dashed line), indicating that they cannot be explained by random noise alone. We further observe that rainfall severity varies most strongly over the 2,000–8,000-day range (5–22 years), which may reflect the influence of long-term climate variability. By contrast, rainfall intensity shows pronounced oscillations over the 2,000–4,000-day range (5–11 years) and the 10,000–15,000-day range (27–41 years), suggesting that extreme rainfall in the region is modulated by at least two distinct climatic drivers. Shorter-period fluctuations are likely associated with regional or local atmospheric processes, whereas longer-period variations may be linked to broader climate forcing.

https://doi.org/10.5194/egusphere-2026-2470
Preprint. Discussion started: 25 August 2026

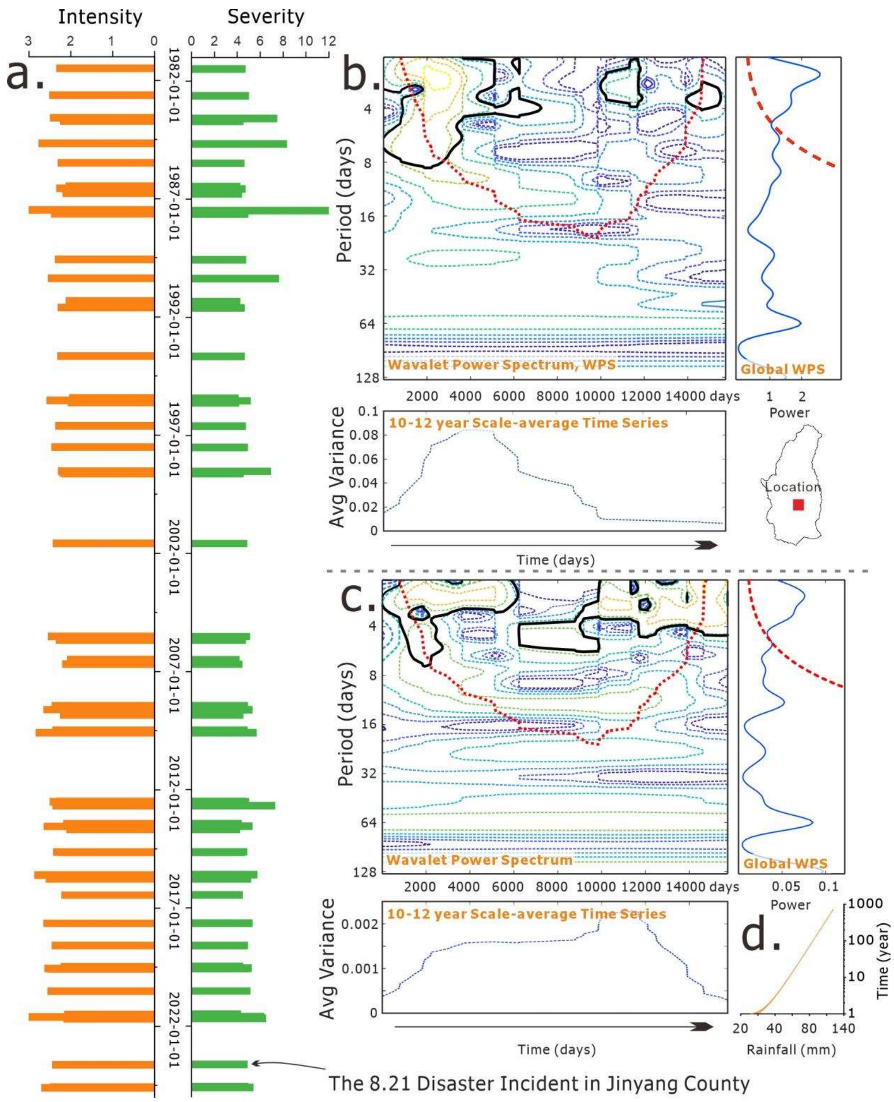

Fig. 9 Characteristics of Historical Extreme Precipitation Events: a, Intensity and severity of extreme precipitation events; **b,** Wavelet power spectrum of extreme precipitation intensity; **c,** Wavelet power spectrum of extreme precipitation severity.

https://doi.org/10.5194/egusphere-2026-2470
Preprint. Discussion started: 25 August 2026

5 Discussion

5.1 Potential Runoff During the Disaster and Human-Disaster Interactions

Based on field measurements in the disaster reach, the average channel slope is 67.7‰ (Fig. 6i). Although flow velocities under different Manning roughness scenarios are illustrated in Fig. 6, direct measurement of Manning's roughness coefficient after the event was not feasible because post-disaster engineering works substantially altered the original channel morphology. During field investigation, the maximum water level observed in the disaster reach was approximately 608 m above sea level, corresponding to a maximum flow depth of about 8 m above the channel bed. The corresponding mean water level was 601.3 m. Using 601.3 m as the validation reference, we found that when Manning's roughness coefficient was set to n=0.18n = 0.18n=0.18, the simulated water level was 601.01 m (Fig. 6j), closely matching the measured mean water level. Under this scenario, the corresponding mean flow velocity was 2.83 m/s. As Manning's roughness coefficient is strongly influenced by bed-material grain size, channel morphology, vegetation cover and human disturbance, including debris accumulation (Phillips and Tadayon, 2007), the inferred value of n=0.18n = 0.18n=0.18 provides important information about channel conditions during the event. In highly irregular natural channels, Manning's roughness typically exceeds 0.11 only where coarse gravel deposits, complex channel morphology and dense vegetation are present simultaneously (Arcement and Schneider, 1989). Thus, a value of n=0.18n = 0.18n=0.18 suggests that the channel was in an exceptionally obstructed state during the disaster, markedly different from that of a relatively unobstructed natural mountain stream. To evaluate whether human activity contributed to this condition, we examined Sentinel-2 multispectral imagery acquired in August during 2019–2024. Comparison of the Normalized Difference Built-up Index (NDBI) (Fig. 10) reveals a clear increase in built-up features after 2021, with mean NDBI rising to 0.054 and peaking at 0.076 in 2023. These observations suggest that human construction activity within or adjacent to the channel likely contributed to flow obstruction and enhanced water-level rise. Under these conditions, water level in the disaster reach rose to approximately 608 m, with a maximum flow depth of about 8 m above the bed. Two distinct flood peaks were identified, with peak discharge periods occurring from 16:00 to 24:00 on 19 August 2023 and from 20:00 on 20 August onward, with corresponding peak discharges of 436 m^3/s and 487 m^3/s, respectively. However, Chen et al.'s research on this incident indicates that the estimated flow rate is 483.42 m^3/s (Chen et al., 2025). The high consistency of the results obtained by different methods further enhanced the credibility of this estimate. Mean flow velocities during these peak periods reached approximately 3.3 m/s–and 3.4 m/s. These results indicate that buildings and channel obstruction may have produced a reduced-velocity–elevated-stage effect, which not only prolonged flood-peak duration but also enhanced the likelihood of overbank flow, thereby amplifying disaster impacts. In this sense, the event reveals clear feedback between human engineering activity and natural hazard processes.

https://doi.org/10.5194/egusphere-2026-2470
Preprint. Discussion started: 25 August 2026

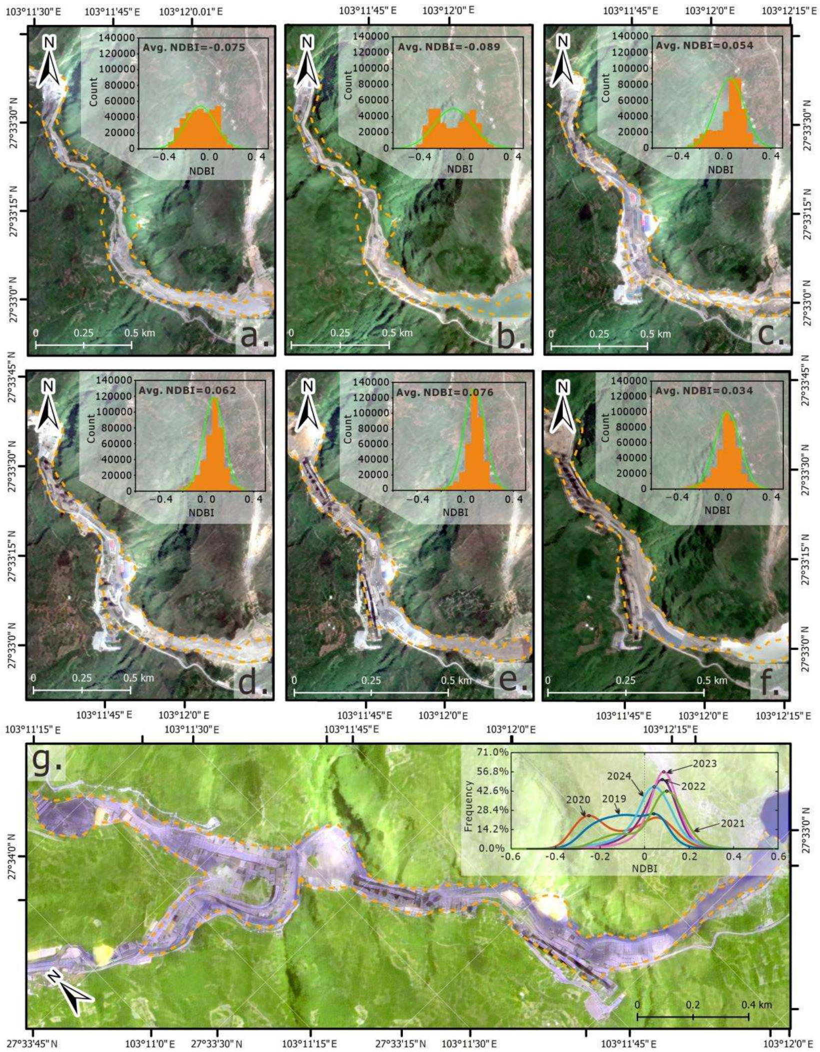

Fig. 10 Interannual Changes in Disaster River Segment Imagery and Building Characteristics: a, Sentinel-2 imagery from August 10, 2019, with NDBI values for the riverbed; **b,** August 27, 2020; **c,** August 4, 2021; d, August 14, 2022; **e,** August 9, 2023; **f,** August 1, 2024; **g,** Shortwave infrared 2, shortwave infrared 1, and red band combination from August 9, 2023, with the frequency curve of recent NDBI values. (Note: The shortwave infrared and red band combination is used for enhanced building detection.)

https://doi.org/10.5194/egusphere-2026-2470
Preprint. Discussion started: 25 August 2026

5.2 Uncertainty and robustness in sediment transport and source estimation

The generation of sediment sources and the magnitude of erosion are controlled jointly by the long-term antagonism between tectonic uplift and fluvial incision and by the spatial organization of erosion and deposition within the channel network. The transient hydrodynamic processes during the disaster represent the short-term concentration of multiple interacting mechanisms and therefore inherently involve substantial uncertainty. Accordingly, although sediment fluxes were estimated in this study (Fig. 7), the true magnitude of erosion may still contain systematic bias.

Three main sources of uncertainty should be acknowledged. First, model assumptions inevitably simplify geomorphic complexity. In particular, the relationship between surface connectivity and sediment transport rate is derived under idealized conditions, and the available hydrological records were collected from surrounding basins (Fig. 7a), which can only approximate the developmental characteristics of comparable geomorphic units. Second, rainfall exhibits strong spatiotemporal heterogeneity, whereas the available forcing data cannot fully resolve hydrodynamic behaviour at very short timescales or at very fine spatial resolution. Third, although InSAR provides high-precision observations of surface deformation, it cannot replace direct experimental or field-based observations of erosional processes and therefore serves mainly as an indirect indicator of erosion extent and slope response.

Despite these limitations, the major patterns of sediment supply and export can still be constrained with reasonable confidence because sediment is derived from both long-term erodibility above the local erosion base level and rainfall-triggered surface erosion. At the valley-system scale, tributaries R5–R9 represent the principal disequilibrium reaches in terms of uplift–incision antagonism and are characterized by relatively rapid uplift, strong bedrock incision and the exposure of Neoproterozoic and Sinian shale–siltstone strata (Fig. 11). Together with surface-derived sediment supply, these conditions form a prominent sediment-source zone (Fig. 7h). Within this zone, the alternation of tectonic-dominated and incision-dominated reaches (Fig. 3) promotes positive feedback of the form bedrock incision → slope steepening → further incision, progressively preconditioning the landscape for block failure.

At the surface, InSAR observations show that deformation rates on shady slopes, particularly north- and northeast-facing slopes, increased markedly after the extreme rainfall event, reaching values up to about three times higher than pre-event levels and substantially exceeding those on sunny slopes. In addition, zones of strong deformation coincide spatially with highly erodible strata (Figs. 8d and 11a), indicating that lithological weakness and rainfall-triggered destabilization act together to promote sediment production. This dual contribution from bedrock and surficial sources probably helps explain the observed offset between sediment peak and water peak (Fig. 6g). During the initial phase of rainfall, readily mobilized surficial sediment, particularly from shady slopes, may enter the system rapidly and generate an early sediment pulse. As runoff subsequently intensifies, additional material derived from bedrock-controlled channel erosion is transported downstream, producing a later hydrological peak.

https://doi.org/10.5194/egusphere-2026-2470
Preprint. Discussion started: 25 August 2026

The reliability of the estimated erosion scale is further constrained by the mapped spatial differentiation between incision and deposition. Seventy-two percent of the channel reaches in the main tributary valleys are characterized by high stream-power gradients and are concentrated in zones of abrupt slope change, whereas the transition zone upstream of the disaster site functions as an energy-dissipation reach, within which depositional segments account for 28% of the total channel length. This pattern limits the efficiency of sediment export from incision-dominated reaches, particularly where the longitudinal valley profile is irregular. In addition, the positive relationship between the bedrock erosion-susceptibility correction factor and the hillslope erodibility factor (Fig. 11b) suggests comparable erodibility of valley-side surface materials and bedrock channel materials. This consistency implies that thick accumulations of highly erodible weathered material are limited and that total sediment supply is correspondingly constrained. Overall, these independent lines of evidence are consistent with our estimate of relatively low sediment-transport flux.

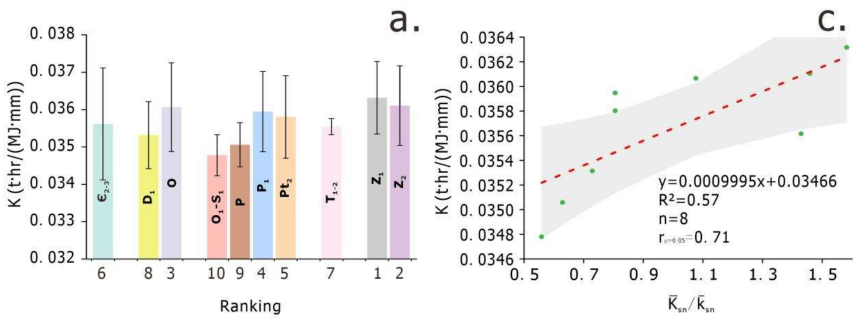

Fig. 11 Differences in the Average K Erosion Factor Across Different Lithological Zones: (a) Differences in the average *K*-values across different rock units; (b) Relationship between the average *K* values and the ratio of $\overline{K}_{sn}/\overline{k}_{sn_t}$).

5.3 Does a weak equilibrium between tectonic uplift and fluvial incision imply hazard risk?

The antagonism between tectonic uplift and fluvial incision is a fundamental driver of topographic development in orogenic belts and underpins the emergence of complex landforms (Xie et al., 2024; Rao et al., 2025; Moumeni et al., 2025). Because this relationship tends toward, but does not necessarily attain, geomorphic equilibrium, it also reflects the self-organizing character of landscape evolution (Xie et al., 2024; Rao et al., 2025). Torrent events can be viewed as short-lived but intense manifestations of this long-term antagonism, raising an important question: can the degree of equilibrium or disequilibrium between tectonic uplift and fluvial incision provide information relevant to hazard identification and early warning? Erosion is generally more active in rapidly uplifting mountain belts such as the Himalaya, Andes, European Alps and Hindu Kush–Pamir. In many cases, higher uplift rates are associated with larger k_{sn} values, steeper channel gradients and greater fluvial incision capacity, thereby promoting sediment production and export. However, the relationship between uplift and erosion is not simply or uniformly positive. In our case, Fig. 12a–d suggests that k_{sn} = 400 $m^{0.9}$ may represent a threshold separating two distinct regimes in the relationship between tectonic forcing and sediment flux. Within a moderate range of relative

https://doi.org/10.5194/egusphere-2026-2470
Preprint. Discussion started: 25 August 2026

uplift rates, erosion activity increases with increasing uplift. Yet where relative tectonic uplift becomes too high, erosion becomes more variable and may even show a negative relationship with uplift. This pattern suggests that the geomorphic effect of uplift is not monotonic. One possible explanation is that rapid uplift in structurally rigid bedrock creates fault-bounded or fracture-controlled topographic surfaces that reduce upstream channel gradients, weaken sediment-routing connectivity and promote local sediment storage. Under such conditions, fluvial incision may locally outpace uplift, causing

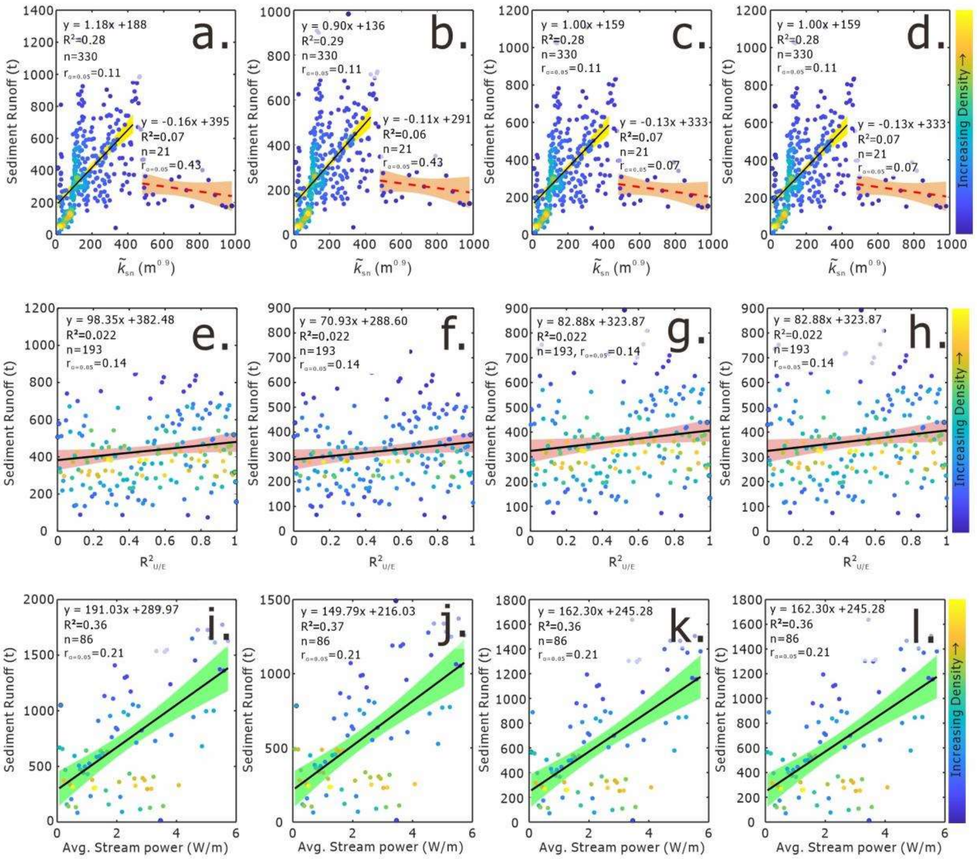

Fig. 12 Relationship Between Tectonic Uplift, Stream Power, Uplift-incision Equilibrium, and Sediment Flux: *a*, k_{sn} vs. sediment flux for $k = 1$, $IC_0 = 0.5$; ***b*,** k_{sn} vs. sediment flux for $k = 1$, $IC_0 = 2$; **c,** k_{sn} vs. sediment flux for $k = 2$, $IC_0 = 0.5$; ***d*,** k_{sn} vs. sediment flux for $k = 2$, $IC_0 = 2$; ***e*,** $R^2_{U/E}$ vs. sediment flux for $k = 1$, $IC_0 = 0.5$; ***f*,** $R^2_{U/E}$ vs. sediment flux for $k = 1$, $IC_0 = 0.5$; ***g*,** $R^2_{U/E}$ vs. sediment flux for $k = 1$, $IC_0 = 0.5$; ***h*,** $R^2_{U/E}$ vs. sediment flux for $k = 1$, $IC_0 = 0.5$; ***i*,** $R^2_{U/E}$ vs. sediment flux for $k = 1$, $IC_0 = 0.5$; ***j*,** Stream power vs. sediment flux for $k = 1$, $IC_0 = 2$; ***k*,** Stream power vs. sediment flux for $k = 2$, $IC_0 = 0.5$; ***l*,** Stream power vs. sediment flux for $k = 2$, $IC_0 = 2$.

$R^2_{\mathrm{U/E}}$ to decline and shifting the system away from weak equilibrium. The result is enhanced stream power, stronger incision and more efficient sediment-transfer pathways. In this sense, the relatively efficient sediment-routing conditions and pronounced disequilibrium near the disaster site suggest that uplift–incision disequilibrium may have diagnostic value for torrent hazards. Figure 12e–h further shows a weak positive relationship between $R^2_{\mathrm{U/E}}$ and sediment flux. This indicates that as tectonic uplift and fluvial incision approach equilibrium along the longitudinal profile, sediment export may increase, although the magnitude of this effect is smaller than that associated with the combined influence of tectonic forcing and fluvial adjustment. Sensitivity analyses involving changes in k and IC_0 indicate that modifying sediment transportability and flux concentration does not fundamentally alter these relationships, suggesting that the observed pattern is relatively robust. For the present event, the large spatial fluctuations in incision and deposition appear to have been the direct geomorphic precondition for disaster occurrence, whereas incision intensity, tectonic activity and their disequilibrium contributed in a hierarchical manner, with progressively decreasing influence from the former to the latter.

5.4 Future Low-Risk Time Windows: When Will They Occur?

Under ongoing climate warming, short-duration extreme rainfall events are increasingly associated with mountain floods, torrent hazards and urban flooding. Because a substantial proportion of the global population lives in mountainous terrain (Ombadi et al., 2023), such events pose growing risks to human life and infrastructure. Although extreme rainfall has traditionally been interpreted through the Clausius–Clapeyron framework, under which atmospheric moisture-holding capacity increases by about 7% per 1°C warming, observations show that short-duration rainfall extremes in some regions increase faster than this baseline expectation (Da Silva and Haerter, 2025). In addition, the synchrony of compound climate extremes has increased globally over recent decades, further increasing systemic hazard pressure (Tang et al., 2025). The study area is embedded within this broader climatic context. This raises a practical question: when might similarly hazardous, or potentially more severe, events recur, and are there identifiable periods of relatively lower or higher climatic favourability for such events in the future? Our results indicate that extreme rainfall in the region exhibits two pronounced quasi-cycles, at approximately 5–11 years and 27–41 years (Fig. 9). These cycles may provide a preliminary basis for identifying future periods of enhanced climatic favourability for hazard occurrence. In the near term, global warming is unlikely to fully reorganize the regional weather systems that trigger extreme rainfall, such as tropical disturbances and low-pressure systems. Under these conditions, the 5–11-year quasi-cycle may remain useful for identifying near-future periods of elevated hazard pressure. By contrast, at longer timescales, the cumulative influence of anthropogenic forcing and climate change is likely to increase uncertainty, making direct extrapolation from the 27–41-year cycle less reliable. For this reason, projections under multiple future socioeconomic pathways (SSP1-2.6, SSP2-4.5, SSP3-7.0 and SSP5-8.5) are needed to assess future changes in extreme-rainfall behaviour.

By comparing projected changes in the frequency, severity, intensity and annual totals of extreme rainfall under different emission scenarios, we find that low-emission pathways are generally associated with lower frequency and severity of

https://doi.org/10.5194/egusphere-2026-2470
Preprint. Discussion started: 25 August 2026

extremes, whereas medium- to high-emission pathways show marked increases in both. Under the most extreme emission pathway, hydroclimatic instability becomes particularly pronounced. In the near term, assuming future development follows a trajectory broadly comparable to SSP1-2.6, and considering the 5–11-year quasi-cycle, strong extreme-rainfall events may still occur during 2026–2035. Over longer timescales, the influence of climate change becomes stronger, and the probability of extreme rainfall increases substantially during 2066–2095, suggesting a higher likelihood of severe hazard events in that period. By contrast, the interval 2046–2055 appears to represent a comparatively lower-risk window across all considered scenarios. These projections should be interpreted as relative shifts in climatic favorability for hazard occurrence rather than deterministic forecasts of future disasters.

https://doi.org/10.5194/egusphere-2026-2470
Preprint. Discussion started: 25 August 2026

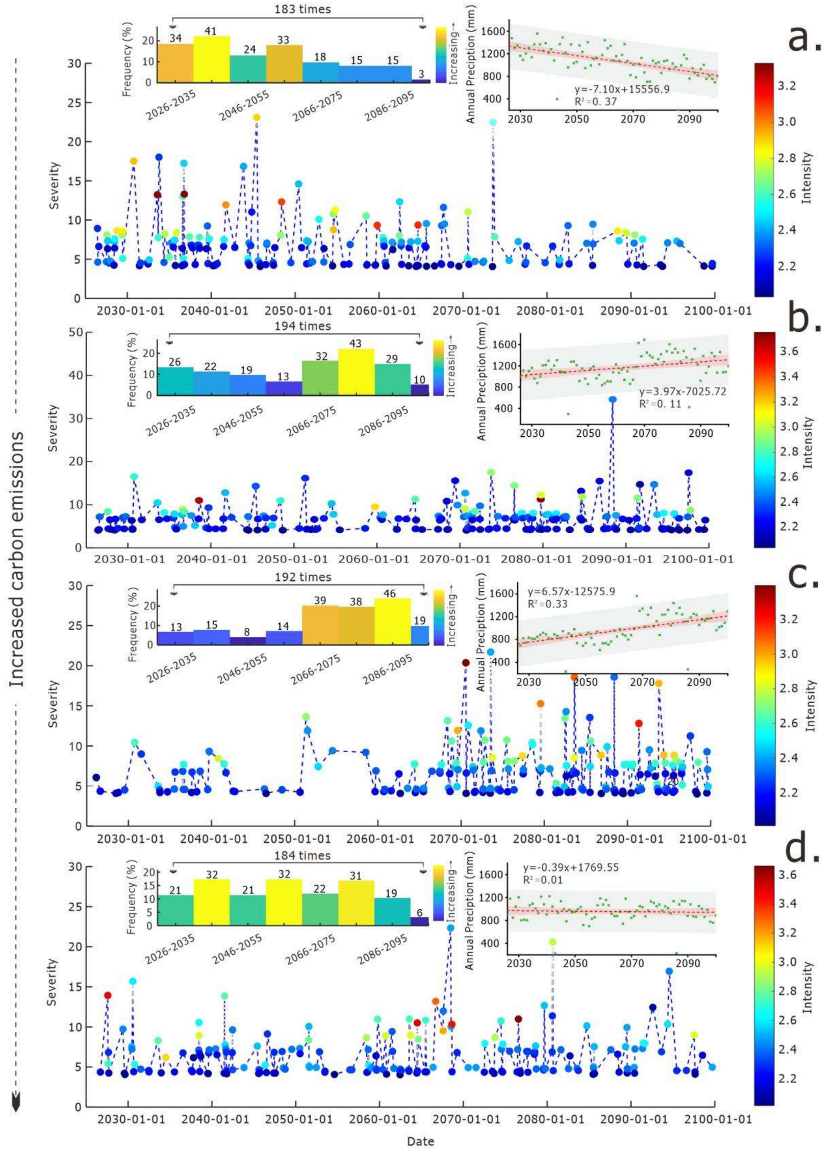

Fig. 13 Extreme Precipitation Events from 2026 to 2099 in Different Carbon Emission Scenarios: *a*, SSP 1-2.6 low-carbon scenario; ***b*,** SSP 2-4.5 moderate-carbon scenario; ***c*,** SSP 3-7.0 high-carbon scenario; ***d*,** SSP 5-8.5 very high-carbon scenario.

https://doi.org/10.5194/egusphere-2026-2470
Preprint. Discussion started: 25 August 2026

5.5 Limitations and broader applicability

This study should be interpreted in light of several limitations. First, the analysis is based on a single representative torrent event in a tectonically active mountain catchment. Although the event provides an informative natural case for examining the coupling between long-term geomorphic forcing and short-term hazard response, the broader transferability of the proposed weak-equilibrium framework requires validation across additional catchments and event types. Second, several key thresholds identified in this study, including the weak-equilibrium window and the apparent ksn transition, are empirical and case-dependent. Their physical meaning and regional applicability should therefore be tested in future work using larger comparative datasets. Third, part of the analysis relies on proxy or substitute datasets, including ERA5-Land precipitation, hydrological records from nearby basins, and InSAR-derived deformation fields. These datasets provide valuable regional constraints, but they cannot fully resolve local hydrodynamic or erosional processes at very short temporal or fine spatial scales. Accordingly, the present results are best interpreted as a mechanistic and data-constrained framework for hazard understanding, rather than as a deterministic prediction model. Despite these limitations, the study provides an important step towards linking long-term uplift–incision antagonism with short-term torrent dynamics. In this sense, the DGR framework may offer a transferable perspective for identifying gynomorphically sensitive settings in tectonically active mountain regions, while future multi-catchment validation will be essential for testing its predictive potential.

6 Conclusions

In the trend of global warming, the frequency of extreme rainfall events has increased, intensifying the tectonic uplift-fluvial incision counteracting effects in mountainous regions. This study investigated the 21 August 2023 torrent disaster in the lower Jinsha River region to examine how extreme rainfall interacts with the long-term antagonism between tectonic uplift and fluvial incision. The results show that the affected catchment is characterized by strong spatial variability in uplift–incision coupling, with the disaster reach located in a geomorphic setting dominated by fluvial incision and marked by uplift–incision disequilibrium. On this basis, we propose the concept of a weak equilibrium window between tectonic uplift and fluvial incision, and show that it may have value for identifying potential hazard-prone settings. Hydro-sedimentary simulations indicate that the event was primarily flood-dominated rather than sediment-dominated, with relatively low sediment fluxes and sediment supply derived mainly from near-source erosion. Two major flood peaks (Flows, ~436 m^3/s and 487m^3/s; velocity, 3.2 and 3.3 m/s) occurred during the event, and field-constrained hydraulic reconstruction suggests that channel obstruction associated with human engineering activity enhanced water-level rise, prolonged flood peaks, and amplified hazard impacts. These results highlight the coupled influence of geomorphic forcing, extreme rainfall and human disturbance on torrent processes. At the climatic scale, extreme rainfall in the region appears to be modulated by two quasi-cyclic modes, at approximately 5–11 years and 27–41 years. When combined with future emission scenarios, these cycles suggest that 2046–2055 may represent a comparatively lower-risk period, whereas stronger hazard pressure may re-emerge in later decades under intensified climate forcing. Overall, the DGR framework developed here provides a transferable approach for linking long-term geomorphic evolution with short-term hazard dynamics, and offers a practical basis for torrent-hazard assessment and risk reduction in tectonically active mountain regions. Its broader predictive applicability, however, remains to be evaluated through multi-catchment comparisons and future event validation.

Data availability

The data underlying this study are available upon request to the corresponding author.

Author contributions

ZG was responsible for constructing the indicator system, conducting data analysis, producing visualizations, and drafting the manuscript; XY provided field investigation data related to the "8.21" disaster event in Jinyang County; XZ and JL contributed soil data.

Competing interests

The contact author has declared that none of the authors has any competing interests.

Acknowledgements

The authors are particularly thankful to the esteemed reviewers for sharing their professional/thoughtful remarks during the evaluation process.

Financial support

This research has been supported by the National Natural Science Foundation of China (grant no. 42107218), the Research Fund of the Institute of Geomechanics (grant no. 2511), the Project Gorges Corporation (grant no. YMJ(BHT)/(21)036), the China Geological Survey Project (grant no. DD20230433), China Geological Survey Project (grant no. DD20230433), Project of Ministry and Province Cooperation, China (Sichuan Geohazard, grant no. 2023ZRBSHZ049) and the Youth Innovation Promotion Association of the Chinese Academy of Sciences (grant no. 2023327).

References

ADREM, SNSE, NDRC, and IRDR: 2021 Global Natural Disaster Assessment Report, Academy of Disaster Reduction and Emergency Management, Ministry of Emergency Management - Ministry of Education; School of National Safety and

Emergency Management, Beijing Normal University; National Disaster Reduction Center of China, Ministry of Emergency Management; International Federation of Red Cross and Red Crescent Societies, Beijing, 2022.

Arcement, G. J. and Schneider, V. R.: Guide for Selecting Manning's Roughness Coefficients for Natural Channels and Flood Plains, U.S. Geological Survey, United States, https://doi.org/10.3133/wsp2339, 1989.

Bekalo, D. J., Bojer, A. K., Al-Quraishi, A. M. F., Debelee, T. G., Negera, W. G., Woldesillasie, F. F., and Esubalew, S. Z.: Geospatial Analysis and Revised Universal Soil Loss Equation (RUSLE) for Predicting Soil Erosion: A Case Study in Deder District, Oromia, Ethiopia, Advances in Space Research, https://doi.org/10.1016/j.asr.2025.07.005, 2025.

Bi, C., Ren, B., and Zheng, J.: Asymmetric effects of ENSO on precipitation in the western north pacific during the follow summer, Journal of Tropocal Meteorology, 39, 89-101 (In Chinese with Chinese Abstract), 2023.

Borselli, L., Cassi, P., and Torri, D.: Prolegomena to sediment and flow connectivity in the landscape: A GIS and field numerical assessment, Catena, 75, 268-277, 2008.

Cai, J., Zhang, L., Dong, J., Guo, J., Wang, Y., and Liao, M.: Automatic identification of active landslides over wide areas from time-series InSAR measurements using Faster RCNN, International Journal of Applied Earth Observation and Geoinformation, 124, 103516, 2023.

Chen, S., Li, J., Yuan, F., Li, L., Song, C., and Deng, Y.: Petrogenetic and tectonic implications of mid-Neoproterozoic I-type granites in the Feidong Complex on the northeastern margin of the Yangtze Block, South China, Journal Of Asian Earth Sciences, 270, 106194, 2024.

Chen, X., Tian, S., Chen, N., Hu, G., Hou, R., and Peng, T.: Why did localized extreme rainfall trigger a rare mega flash flood in the mountains of western China?, International Journal of Disaster Risk Reduction, 116, 105090, 2025.

Chen, Z., Wang, L., Li, X., Xue, Y., and Jia, H.: Spatiotemporal Change Characteristics of Extreme Precipitation in South - western China and its Relationship with Intense ENSO Events, Plateau Meteorology, 41, 604-616 (In Chinese with English Abstract), 2022.

Da Silva, N. A. and Haerter, J. O.: Super-Clausius–Clapeyron scaling of extreme precipitation explained by shift from stratiform to convective rain type, Nature Geoscience, https://doi.org/10.1038/s41561-025-01686-4, 2025.

Delchiaro, M., Seta, M. D., Martino, S., Nozaem, R., and Moumeni, M.: Tectonic deformation and landscape evolution inducing mass rock creep driven landslides: the Loumar case-study (Zagros Fold and Thrust Belt, Iran), Tectonophysics, 846, 229655, 2023.

Delchiaro, M., Seta, M. D., Martino, S., Moumeni, M., Nozaem, R., Marmoni, G. M., and Esposito, C.: The role of long-term preparatory factors in mass rock creep deforming slopes: insights from the Zagros Mts. belt (Iran), Landslides, 21, 1735-1755, 2024.

Demoulin, A., Mather, A., and Whittaker, A.: Fluvial archives, a valuable record of vertical crustal deformation, Quaternary Science Reviews, 166, 10-37, 2017.

Dong, J., Zhou, Y., and You, N.: The 30-meter annual maximum NDVI dataset of China from 2000 to 2021, National Ecosystem Science Data Center [dataset], https://doi.org/10.12199/nesdc.ecodb.rs.2021.012, 2021.

Du, L., Guo, J., P.Nutman, A., Wyman, D., Geng, Y., Yang, C., Liu, F., Ren, L., and Zhou, X.: Implications for Rodinia reconstructions for the initiation of Neoproterozoic subduction at ~860 Ma on the western margin of the Yangtze Block:Evidence form the Guandaoshan Pluton, Lithos, 196-197, 67-82, 2014.

Edwards, D. C.: Characteristics of 20th Century Drought in the United States at Multiple Time Scales, Department of Atmospheric Science, Colorado State University, Fort Collins, 1997.

Farahmand, A. and AghaKouchak, A.: A generalized framework for deriving nonparametric standardized drought indicators, Advances in Water Resources, 76, 140-145, 2015.

Fienen, M. N., Doherty, J. E., Hunt, R. J., and Reeves, H. W.: Using Prediction Uncertainty Analysis to Design Hydrologic Monitoring Networks: Example Applications from the Great Lakes Water Availability Pilot Project, U.S. Department of the Interior
U.S. Geological Survey, Reston, Virginia, 2010.

Gu, Z., Shi, C., and Peng, J.: Evolutionary dynamics of the main-stem longitudinal profiles of ten kongdui basins within Inner Mongolia, China, Journal of Geographical Sciences, 29, 417-431, 2019.

Gu, Z., Yao, X., and Zhu, X.: Debris Flow Susceptibility in the Jinsha River Basin, China: A Bayesian Assessment Framework based on
Geomorphodynamic Parameters, Natural Hazards and Earth System Sciences, 25, 3957-3975, 2025.

Gu, Z., Yao, X., Chuangchuang Yao, and Li, C.: Mapping of geomorphic dynamic parameters for analysis of landslide hazards: a case of Yangbi river basin on the upper Lancang-Mekong of China, Journal of Mountain Science, 18, 2402-2411, 2021.

Gu, Z., Yao, X., Li, C., and Zhu, X.: Driving effects of dynamic geomorphologic environments on gravitational erosion hazards: a case of the Baihetan drainage area of the Jinsha River, China, Bulletin of Engineering Geology and the Environment, 82, 1-16, 2023.

Guo, C., Ning, N., Guo, H., Tian, Y., Bao, A., and Maeyer, P. D.: Does ERA5-Land Effectively Capture Extreme Precipitation in the Yellow River Basin?, Atmosphere, 15, 1254, 2024.

Gupta, P., Khanna, A., and Majumdar, S.: Disaster Management in Flash Floods in Leh (Ladakh): A Case Study, Indian Journal of Community Medicine, 37, 185-190, 2012.

Huang, S., Zhang, X., Chen, N., Li, B., Ma, H., Xu, L., Li, R., and Niyogi, D.: Drought propagation modification after the construction of the Three Gorges Dam in the Yangtze River Basin, Journal of Hydrology, 603, 127138, 2021.

Jaafar, H. H., FarahA.Ahmad, and Beyrouthy, N. E.: GCN250, new global gridded curve numbers for hydrologic modeling and design, Scientific Data, 2019, 145, 2019.

Kirby, E. and Whipple, K.: Quantifying differential rock-uplift rates via stream profile analysis, Geology, 29, 415-418, 2001.

Li, R., Wang, P., Tan, S., Zhou, Y., Liu, L., Gou, C., and Yu, Y.: Exploration of slope-type geological hazard susceptibility evaluation based on dynamic correction of SBAS-InSAR technology: A case study of Kang County in Gansu Province, Ecological Informatics, 85, 102945, 2025.

https://doi.org/10.5194/egusphere-2026-2470
Preprint. Discussion started: 25 August 2026

Liu, Y. and Gupta, H. V.: Uncertainty in hydrologic modeling: Toward an integrated data assimilation framework, Water Resources Research, 43, W070401, 2007.

Mockus, V.: National engineering handbook, Washington, U.S., 1964.

Moumeni, M., Delchiaro, M., Ballato, P., Seta, M. D., Nozaem, R., Clementucci, R., Tikhomirov, D., Christl, M., and Egli, M.: Coupling of Tectonics, Climate, and Lithology in Orogenic Systems: Insights From Cosmogenic ^{10}Be Erosion Rates and River Profile Inversion Modeling in the Talesh Mountains, NW Iranian Plateau, Tectonics, 84, 15, 2025.

Ombadi, M., Risser, M. D., Rhoades, A. M., and Varadharajan, C.: A warming-induced reduction in snow fraction amplifies rainfall extremes, Nature, 619, 305-310, https://doi.org/10.1038/s41586-023-06092-7, 2023.

Perron, J. T. and Royden, L.: An integral approach to bedrock river profile analysis, Earth Surface Processes and Landforms, 38, 570–576, 10.1002/esp.3302, 2013.

Phillips, J. V. and Tadayon, S.: Selection of Manning's Roughness Coefficient for Natural and Constructed Vegetated and NonVegetated Channels, and Vegetation Maintenance Plan Guidelines for Vegetated Channels in Central Arizona, U.S., Reston, Virginia, 2007.

Rao, W., Liu, B., Feng, T., Wang, Q., and Tang, H.: What is the present-day tectonic uplift rate of the Tibetan Plateau?, Earth & Planetary Science Letters, 662, 119389, 2025.

Räsänen, T. A., Tähtikarhu, M., and Hyväluoma, J.: Exploring the RUSLE-based structural sediment connectivity approach for agricultural erosion management, Catena, 246, 108420, 2024.

Shi, C. and Shao, W.: Knickpoints within the Suoshui watershed and the implication for the age of sandstone pillars in Zhangjiajie, China, Geomorphology, 221, 261-273, 2014.

Snyder, N. P., Whipple, K. X., Tucker, G. E., Tucker, G. E., and Merritts, D.: Landscape response to tectonic forcing: DEM analysis of stream profiles in the Mendocino Triple Junction region, northern California, Geological Society of America Bulletin, 112, 1250-1263, 2000.

Soulis, K. X. and Valiantzas, J. D.: SCS-CN parameter determination using rainfall-runoff data in heterogeneous watersheds – the two-CN system approach, Hydrology and Earth System Sciences, 16, 1001-1015, 2012.

Su, Q., Yuan, D., Zhang, H., Manopkawee, P., Zhan, Y., Zhang, P., and Xie, H.: Geomorphic evidence for northeastward expansion of the eastern Qilian Shan, northeastern Tibetan Plateau, Journal of Asian Earth Sciences, 177, 314-323, 2019.

Sun, L., Liu, F., Zhu, X., and Zhang, G.: High-resolution digital mapping of soil erodibility in China, Geoderma, 444, 116853, 2024a.

Sun, Y., Li, R., Liu, B., Zhao, X., Shi, H., Li, H., Ren, Y., Fan, X., Dong, L., Xu, Y., Chang, Y., Yuan, L., Yang, Q., and Zhang, H.: A new high-resolution global topographic factor dataset calculated based on SRTM V3 (2015) [dataset], https://doi.org/10.11888/Terre.tpdc.300613, 2023.

Sun, Y., Zhang, H., Yang, Q., Li, R., Liu, B., Zhao, X., Shi, H., Li, H., Ren, Y., Fan, X., Dong, L., Xu, Y., Chang, Y., and Yuan, L.: A new high-resolution global topographic factor dataset calculated based on SRTM, Scientific Data, 11, 1-18, 2024b.

https://doi.org/10.5194/egusphere-2026-2470
Preprint. Discussion started: 25 August 2026

Tang, Y., Luo, M., Wu, S., and Li, X.: Increasing synchrony of extreme heat and precipitation events under climate warming, Geophysical Research Letters, 52, e2024GL113021, 2025.

Times, G.: Heavy rain leaves 4 dead, 48 missing in China's Sichuan, 2023a.

Times, T. S.: Heavy rain leaves 4 dead, 48 missing in China’s Sichuan, 2023b.

Vigiak, O., Borselli, L., Newham, L. T. H., McInnes, J., and Roberts, A. M.: Comparison of conceptual landscape metrics to define hillslope-scale sediment delivery ratio, Geomorphology, 138, 74-88, 2012.

Wang, M., Zhao, Y., Shi, W., Yu, J., Chen, T., Bao, J., Song, W., and Chen, H.: A modified curve number method for runoff prediction of different soil types in China, Catena, 254, 108957, 2025.

Wang, Y., Zhang, H., Zheng, D., Dassow, W. V., Zhang, Z., Yu, J., and Pang, J.: How a stationary knickpoint is sustained: New insights into the formation of the deep Yarlung Tsangpo Gorge, Geomorphology, 285, 28-43, 2017.

Wei, L., Hu, K., Liu, S., Ning, L., Zhang, X., Zhang, Q., and Rahim, M. A.: The vulnerability of buildings to a large-scale debris flow and outburst flood hazard cascade that occurred on 30 August 2020 in Ganluo, southwest China, Natural Hazards And Earth System Sciences, 24, 4179-4197, 2024.

Wen, Q., He, G., and Yang, H.: Comparison Studies of the Effect of Tibetan Plateau and Rocky Mountains on ENSO Variability, Chinese Journal of Atmospheric Science, 46, 1209-1224 (In Chinese with English Abstract), 2022.

Xie, Y., Balázs, A., Gerya, T., and Xiong, X.: Uplift of the Tibetan Plateau driven by mantle delamination from the overriding plate, Nature Geoscience, 17, 683-688, 2024.

Xu, H., Shen, J., Yang, F., Hu, Q., Yu, Y., Xiong, L., Zhang, T., a, H. D., and He, J.: Provenance, sedimentary paleoenvironment and organic matter accumulation mechanisms in shales from the Lower Cambrian Qiongzhusi Formation, SW Yangtze Block, China, Marine and Petroleum Geology, 181, 107520, 2025.

Yang, J., Dong, J., Xiao, X., Dai, J., Wu, C., Xia, J., Zhao, G., Zhao, M., Li, Z., Zhang, Y., and Ge, Q.: Divergent shifts in peak photosynthesis timing of temperate and alpine grasslands in China, Remote Sensing of Environment, 233, 111395, 2019.

Yang, W., Zheng, C., Jiang, X., Wang, H., Lian, J., Hu, D., and Zheng, A.: Study on urban flood simulation based on a novel model of SWTM coupling D8 flow direction and backflow effect, Journal of Hydrology, 621, 129608, 2023.

Yao, S., Wang, Q., Mou, C., Ren, P., Zan, B., Xie, S., Liu, J., and Liu, X.: Provenance and tectonic settings of late Triassic–Jurassic deposits in the Southwestern Yangtze block: evidence from the geochemistry, SW China, Scientific Reports, 15, 23237, 2025.

Yevjevich, V.: An objective approach to definitions and investigations of continental hydrologic droughts, Journal of Hydrology, 7, 353, 1969.

Zhang, J., Ding, X., Liu, Y., Liu, P., Shi, C., and Zhang, H.: The ca. 1.13–0.92 Ga magmatism in the western Yangtze Block, South China: Implications for tectonic evolution and paleogeographic reconstruction, Precambrian Research 386, 106961, 2023.

Zhang, J., Jing, L., Scherler, D., Yin, A., Wang, W., Tang, M., and Li, Z.: Spatiotemporal variation of late Quaternary river incision rates in southeast Tibet, constrained by dating fluvial terraces, Lithosphere, 10, 662-675, 10.1130/l686.1, 2018.

Zhou, T.-J., Chen, Z.-M., Chen, X.-L., Zuo, M., Jiang, J., and Hu, S.: Interpreting IPCC AR6: future global climate based on projection under scenarios and on near-term information, Climate Change Research, 17, 652-663 (In Chinese with English Abstract), 2021.